Enhanced selectivity towards melanoma cells with zinc(II)-Schiff bases containing imidazole derivatives

Leonor Côrte-Real[a], Baris Sergi[b]†, Busra Yildirim[b]†, Raquel Colucas[a], Radosław Starosta[a,c], Xavier Fontrodona[d], Isabel Romero[d], Vânia André[a], Ceyda Acilan[b,e]*, Isabel Correia[a]*

[a]Centro de Química Estrutural, Institute of Molecular Sciences, and Department of Chemical Engineering, Instituto Superior Técnico, Universidade de Lisboa, Avenida Rovisco Pais, 1049-001 Lisboa, Portugal

[b]Koç University, School of Medicine, Sariyer, Istanbul, Turkey

[c]Faculty of Chemistry, University of Wrocław, ul. F. Joliot-Curie 14, 50-383 Wrocław, Poland

[d]Departament de Química and Serveis Técnicas de Recerca, Universitat de Girona, Spain

[e]Koç University, Research Center for Translational Medicine (KUTTAM), Istanbul, Turkey

*Correspondence: icorreia@tecnico.ulisboa.pt
†These authors contributed equally to this work.

ABSTRACT

Zinc(II)-complexes with the general formula $[Zn(L)_2]$ containing 8-hydroxyquinoline Schiff bases functionalized with 1-(3-aminopropyl)imidazole or 1-(3-aminopropyl)-2-methyl-1H-imidazole on 2-position and their respective ligands (**HL^1** or **HL^2**) were synthesized and characterized by NMR, UV-Vis, FTIR and CD spectroscopies as well as ESI-MS spectrometry. Single crystals of **HL^2** and **$[Zn(L^1)_2]_n$** were analysed by SC-XRD. **$[Zn(L^1)_2]_n$** shows a 1D polymeric chain structure of alternating Zn(II) cations and bridging Schiff base ligands, in contrast to previously reported monomeric structures of analogous complexes. DFT calculations were performed to rationalize the polymeric X-ray structure of **$Zn(L^1)_2$**. Results showed that the ligands can bind as bi- or tridentate to Zn(II) and there is the possibility of a dynamic behavior for the complexes in solution. Both ligands and complexes present limited stability in aqueous media, however, in the presence of bovine serum albumin the complexes are stable. Molecular docking simulations and circular dichroism spectroscopic studies suggest binding to this protein in close proximity to the Trp213 residue. Biological studies on a panel of cancer cells revealed that the Zn(II)-complexes have a lower impact on cell viability than cisplatin, except for triple-negative breast cancer cells in which they were comparable. Notwithstanding, they display much higher selectivity towards cancer cells *vs.* normal cells, than cisplatin. They induce the generation of ROS and DNA double-strand breaks, primarily through apoptosis as the mode of cell death. Overall, the novel Zn(II)-complexes demonstrate improved induction of apoptosis and higher selectivity, particularly for melanoma cells,

compared to previously reported analogues, making them promising candidates for clinical application.

Keywords: zinc, anticancer metallodrugs, imidazole, 8-hydroxyquinoline, Schiff bases, DFT.

1. INTRODUCTION

Nitrogen heterocycles play a crucial role in medicinal chemistry, serving as a backbone for numerous biologically active compounds. This scaffold has gained significant attention due to its diverse pharmacological properties, and its incorporation into drug molecules has been proven to enhance bioactivity, selectivity, and pharmacokinetic properties [1, 2]. According to FDA databases, approximately 60% of small-molecule drugs contain nitrogen-based heterocycles, highlighting the structural and functional importance of these compounds in drug design and discovery [3].

Quinolines, a class of N-heterocycles, have attracted considerable attention in medicinal chemistry due to their diverse biological activities. Quinoline-based compounds have demonstrated promising anticancer properties, with the ability to interact with various cellular targets, such as DNA, enzymes, and receptors. Moreover, the structural versatility of quinolines allows for the synthesis of a wide range of derivatives, enabling researchers to fine-tune their pharmacological properties and optimize their anticancer activity [4]. Some examples of quinoline-containing drugs that have received FDA approval include Lenvatinib (protein kinase inhibitor for certain kinds of thyroid cancer), Tipifarnib (farnesyl transferase inhibitor for leukemia), and the well-known Irinotecan (enzyme inhibitor primarily used in the treatment of colorectal cancer) – **Fig. 1** [5, 6].

Similarly, imidazoles have also shown great potential as anticancer agents. Imidazole-based compounds exhibit a broad spectrum of biological activities, including antitumor, anti-inflammatory, and antimicrobial properties [7]. The unique structural features of imidazoles, such as their ability to participate in hydrogen bonding and interact with metal ions, contribute to their diverse pharmacological profiles. Furthermore, the presence of nitrogen atoms allows for the introduction of various substituents, enabling the synthesis of structurally diverse compounds with enhanced anticancer activity [7, 8]. Some examples of imidazole-based drugs clinically approved are Temozolomide (alkylating agent used to treat specific types of brain cancer), Mercaptopurine (immunomodulator used to treat acute lymphocytic leukemia) and Dacarbazine (antineoplastic agent used to treat metastatic malignant melanoma and Hodgkin's disease) – **Fig. 1** [9].

The unique physicochemical properties and structural versatility of these nitrogen heterocycles allow the design of compounds with enhanced bioactivity and selectivity, offering new avenues for the development of effective and targeted drugs.

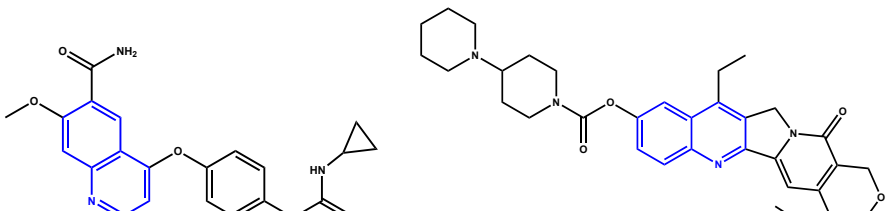

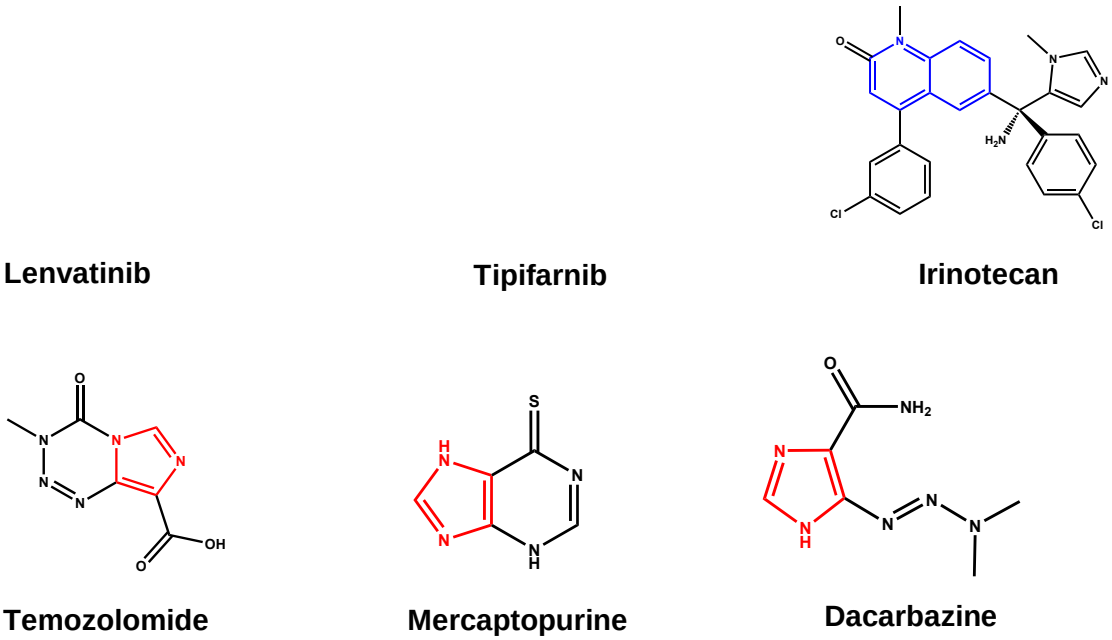

Figure 1. Quinoline-based and imidazole-based drugs clinically approved for cancer therapy.

Our group has recently reported a series of Zn(II)- and Cu(II)-complexes bearing 8-hydroxyquinoline (8HQ) Schiff bases with amines containing morpholine or piperidine moieties [10] (**Fig. 2**). These compounds have shown ability to bind bovine serum albumin (BSA) and to react with relevant cell (glutathione) and plasma (ascorbic acid) reductants. Preliminary cytotoxicity evaluations revealed that all compounds demonstrate significant antiproliferative activity against melanoma cells, with the Cu(II)-complexes being *ca.* 2-fold more cytotoxic than cisplatin, and more active than the Zn(II)-complexes, despite the latter being more selective towards cancer cells.

Encouraged by the above considerations and in line with our ongoing research of anticancer metallodrugs featuring the 8HQ backbone [11-14], we report herein the synthesis, characterization, and biological activity results of novel Zn(II)-complexes incorporating both 8HQ and imidazole moieties, with a focus on their potential as anticancer agents. Our rationale was to merge two biologically active moieties [15] to possibly benefit from synergistic effects/dual modes of action. Moreover, some drugs when administered as metal complexes show increased activity compared to the parent ligands.

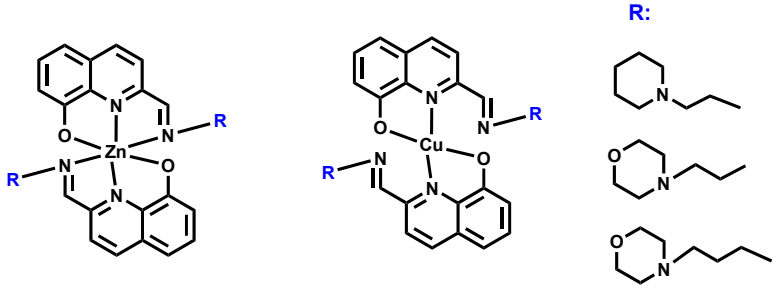

Figure 2. Chemical structure of our previously reported Zn(II)- and Cu(II)-complexes.

2. RESULTS AND DISCUSSION

The Schiff bases were synthesized by a base-catalyzed condensation reaction between 8-hydroxy-2-quinolinecarboxaldehyde (8HQ-2CHO) and amines, 1-(3-aminopropyl)imidazole and 1-(3-aminopropyl)2-methyl-1H-imidazole, yielding **HL¹** and **HL²** precursors, respectively, that were isolated with good yields (*ca.* 80%). The Zn(II)-complexes (**Zn(L¹)₂** and **Zn(L²)₂**) were obtained *in-situ* in a reaction between **HL¹** or **HL²** with $ZnCl_2$ in an ethanolic solution and in the presence of KOH - see **Scheme 1** and **Experimental section**. The final products were isolated pure after recrystallization from CH_2Cl_2/diethyl ether and obtained in moderate yields (*ca.* 50%). The complexes are stable under air and moisture in the solid state, in contrast to the free ligands, which are hygroscopic and, therefore, were stored in sealed ampoules. All ligand precursors and complexes are new and were characterized by elemental analysis (% CHN) and the usual spectroscopic techniques, in the solid state and solution. The final compounds' elemental analyses (**Experimental Section**) and ESI-MS data (**Supplementary Material (SM) - Table S1**) support the expected structural formulae. Single crystals were obtained for ligand **HL²** and complex **Zn(L¹)₂**, allowing the determination of their molecular structures by single-crystal X-ray diffraction (SC-XRD) analysis.

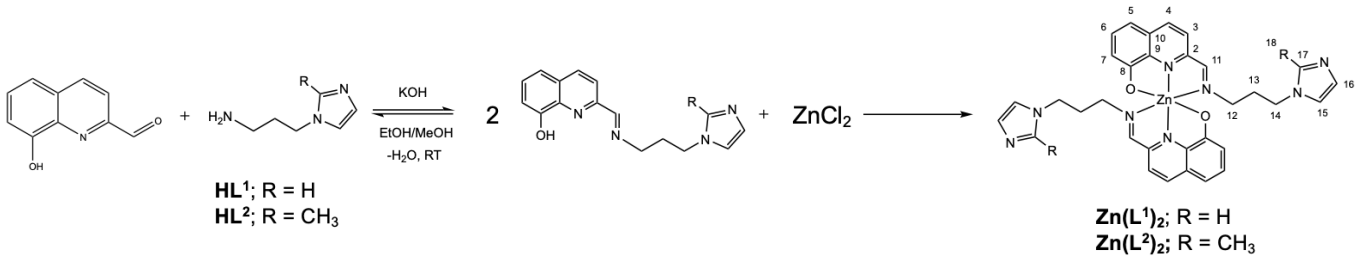

Scheme 1. Outline of the synthesis of the new Schiff bases, **HL¹** and **HL²** and of Zn(II)-complexes **Zn(L¹)₂** and **Zn(L²)₂**. The carbon atoms are numbered for NMR assignment.

2.1. NMR characterization

The ^{1}H and ^{13}C NMR spectra of all compounds were measured in deuterated DMSO (see **Figs. S1-S4**), and the chemical shifts are in good agreement with related compounds [10]. The downfield shifting of the azomethine proton H_{11} (–CH=N–) from δ 8.43 and 8.50 ppm in the ^{1}H NMR spectrum of the free ligands **HL¹** and **HL²** to δ 8.66 and 8.79 ppm in the ^{1}H NMR spectrum of Zn(II)-complexes **Zn(L¹)₂** and **Zn(L²)₂**, respectively, clearly indicates chelation of the azomethine-N atom with the metal ion. These results agree with the conclusions drawn from IR spectral studies (see below). The ^{13}C NMR spectrum of complex **Zn(L²)₂** reveals a similar behavior to related compounds [10], *i.e.*, the hydroxyl carbon (C_8) experiences a downfield shift (from δ 161.57 ppm to 163.21 ppm), while the azomethine carbon (C_{11}) undergoes an upfield shift (from δ 163.51 ppm to 161.44 ppm), compared to the free ligands. For complex

Zn(L^1)$_2$, the shielding effect of C_{11} upon coordination is also observable, providing additional evidence of the coordination of the azomethine nitrogen to the metal center. However, the hydroxyl carbon shows an opposite effect, *i.e.*, an upfield shift, compared to the free ligand (from δ168.67 ppm to 163.56 ppm). This effect can possibly be due to the formation of a polymeric chain (confirmed by SC-XRD in the solid state) and, consequently, the proximity of the imidazole group (that is coordinated with the metal center) to the O-phenolate group of the 8HQ ring, promoting this shielding effect. All the remaining aromatic protons were only slightly affected by metal chelation and are in accordance with the proposed structures.

2.2. UV-Vis characterization

The optical absorption spectra of the ligands and complexes were recorded using 1.0×10^{-5} to 1.0×10^{-4} M solutions in CH_2Cl_2 and/or DMSO. **Fig. 3** compares the spectra of the free ligands and metal complexes in DMSO, whereas **Table S2** presents the values obtained for the molar absorptivity coefficient (ε) and the corresponding maximum wavelength (λ_{max}).

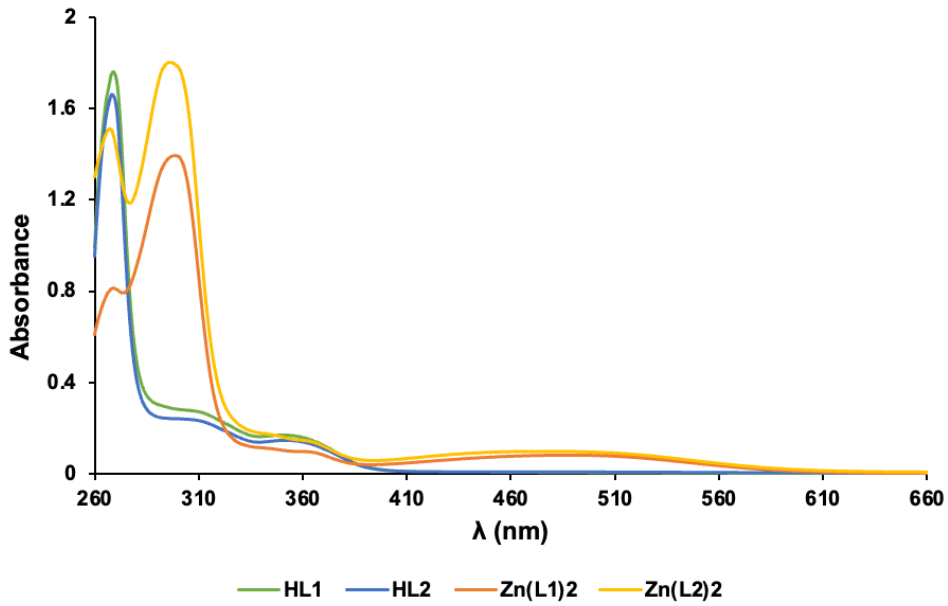

Figure 3. UV-Vis absorption spectra of the ligands (green and blue) and respective Zn(II) complexes (orange and yellow) in DMSO [c = 30−113 μM].

The electronic absorption spectra of the ligands in DMSO show one intense absorption band at ~270 nm (π→π*) and two shoulders in the region 300−400 nm that are assigned to intraligand n→π* transitions of the azomethine group. The π→π* transitions of the aromatic rings of 8HQ are below the cut-off of the solvent but can be observed in methanol (see **Fig. S5** for **Zn(L^1)$_2$** as an example). After complexation, the bands of the Zn(II) complexes suffer a bathochromic shift, indicating coordination of the ligand to the metal through the azomethine moiety [10, 16]. Additionally, one can observe the presence of a broad band in the visible

region that can be ascribed to a charge-transfer band [10, 17]. The spectra are similar for both complexes, indicating similar coordination structures.

2.3. FTIR characterization

The infrared spectra obtained for the free ligands and their corresponding complexes show similar bands to those reported in the literature for complexes containing a Schiff base coupled to an aromatic ring [10, 12, 18]. One of the main bands corresponds to the stretching vibration of the azomethine group, ν(C=N), at 1644 cm^{-1} and 1646 cm^{-1} for **HL¹** and **HL²**, respectively. For the Zn(II)-complexes, this band shifts to lower wavenumbers (1640 cm^{-1} and 1643 cm^{-1} for **Zn(L¹)₂** and **Zn(L²)₂**, respectively), indicating a decrease in the bond order and coordination of the metal to the imine nitrogen lone pair [19, 20].

The bands observed at ~1448 cm^{-1} and 1452 cm^{-1} correspond to the C=C stretching vibrations of the quinoline and of imidazole rings.

The presence of a broad band around 3420 cm^{-1} in the infrared spectra can be attributed to the presence of solvent molecules and the stretching vibrations of the hydroxyl group (in the ligands). This band is more pronounced in the spectra of the ligands also due to their hygroscopic nature.

3.4. Single crystal X-ray diffraction

The structures of **HL²** and **[Zn(L¹)₂]ₙ** were elucidated from single crystal X-ray diffraction data. Crystals of **HL²** were obtained from dichloromethane/diethyl ether, while for **[Zn(L¹)₂]ₙ,** they were recrystallized from DMSO.

HL² (**Fig. 4**) crystallizes in the $P2_1/c$ monoclinic space group (details in the **Experimental Section** and see **Table S3** for the main crystallographic data). The **HL²** structure reveals that bond distances and angles are within the expected values. **HL²** molecules establish intermolecular hydrogen bonds among them via the hydroxyl and the imidazole moieties (O_1-H···N_4, 2.6991(8) Å) giving rise to $C_1^1(14)$ chains (**Table S4**).

A

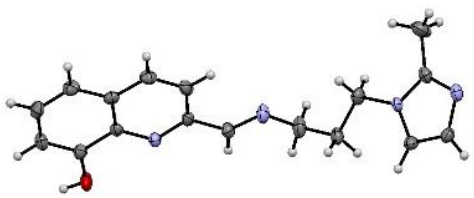

B

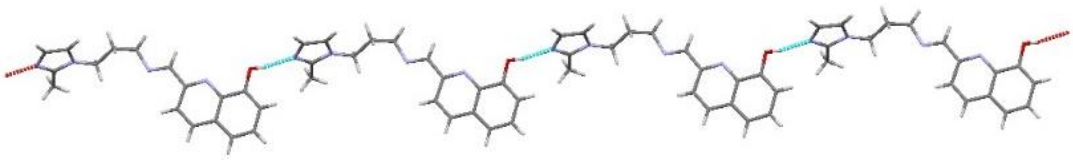

Figure 4. A) Ellipsoid representation of **HL²** structure (ellipsoids set at 50% probability); **B**) $C_1^1(14)$ chains representative of **HL²** supramolecular arrangement, based on O-H···N hydrogen bonds depicted in cyan and red.

Figure 5 displays the ORTEP plot for the X-ray structure of **$[Zn(L^1)_2]_n$** and **Experimental Section** and **Tables S3** and **S5** the main crystallographic data and selected bond distances and angles. The compound crystallizes in the monoclinic system, space group $P12_1/c1$. When the imidazole moiety is incorporated into the 8HQ ligand, the imine nitrogen atoms of both ligands do not coordinate to the metal center to form the corresponding monomer, but rather, the nitrogen atoms of the imidazole moiety are the ones that coordinate, thus forming a 1D polymeric chain structure of alternating Zn(II) cations and bridging Schiff base ligands (**HL¹**) (**Fig. S6**). Two **HL¹** ligands bridge two Zn atoms. Each of the centrosymmetric Zn(II) ions possesses a distorted octahedral geometry, with Zn(II) coordinated by two phenolate O atoms (O1) and two quinoline N atoms (N1), from two 8HQ ligands. The N-donor and the O-donor atoms are located *trans* to each other, similar to other octahedral Zn(II)-complexes containing 8HQ ligands without substituents in the *ortho* position to the quinoline nitrogen [21], since the presence of these substituent lead to preferential *cis* coordination of phenolate O atoms [10]. The other two coordination positions are completed by two imidazolic nitrogen atoms (N4) from two different ligands, that are located *trans*.

The Zn–O bond distances (2.058(3) Å) and Zn–$N_{quinoline}$ bond distances (2.254 Å) are in the same range as other Zn(II) polymers [22] and complexes [23] described in the literature. The Zn–$N_{imidazole}$ bond distances (2.153 Å) are shorter than the Zn–$N_{quinoline}$ ones (2.254 Å). Intramolecular hydrogen bonds between the O atoms and i) H atoms of the imidazole group (O1-H17 = 2.554 Å; O1-H16 = 2.816 Å) and ii) H atoms of the iminic carbon (O1-H11 = 2.294 Å) are displayed along the 1D chain, which has some influence in the geometry of the resulting polymer. Other intermolecular hydrogen bonds are also observed, i) between the O atoms of the DMSO molecules situated between the adjacent 1D chains and H atoms of the imidazole groups (O4S-H15= 2.278 Å) and ii) between the DMSO molecules of solvent (O4S-H3SA= 2.612 Å), (**Fig. S7**).

The supramolecular structure of the polymer shows polymeric alternating linear chains with the DMSO solvent molecules situated between the different chains (**Fig. S8**). However, no π-

stacking interactions between aromatic rings of neighbouring molecules have been observed. Other views of the packing are shown in **Fig. S9**.

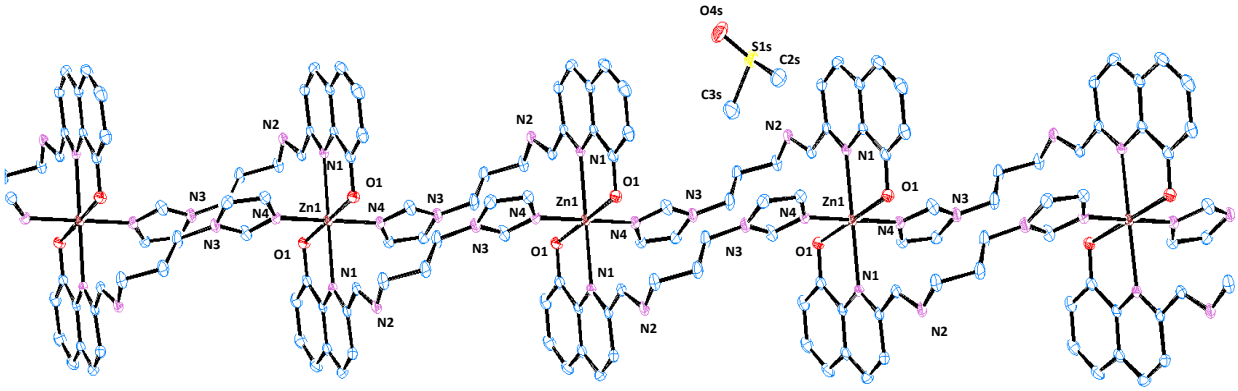

Figure 5. Molecular structure of the Zn(II) polymer **$[Zn(L^1)_2]_n$** determined by SC-XRD.

2.5. Conformational analysis of the complexes by the DFT calculations

DFT calculations (ωB97XD/6-311++G(d,p)) were performed to rationalize the unexpected polymeric X-ray structure of **$Zn(L^1)_2$**. Namely, the expected structures of **$Zn(L^1)_2$** and **$Zn(L^2)_2$** should be similar to the previously reported [10] analogous Zn(II)-complexes bearing 8-hydroxyquinoline Schiff bases with amines containing morpholine or piperidine moieties (**Fig. 2**). This obvious discrepancy shows that **HL^1** and **HL^2** can act as tridentate or bidentate ligands, depending on the relative position of the N atom from the azomethine group (–CH=N–). Our goal was to show possible routes of conformational changes of the "typical" structures leading to formation of the polymeric structure of **$[Zn(L^1)_2]_n$**. For the sake of clarity, most of the calculations were performed for the complexes with 2-((methylimino)methyl)quinolin-8-ol (**HL^0**, **Fig. S10**) - the simplified model of the ligands **HL^1** and **HL^2**. Such an approach also allowed us to obtain more general results, applicable to this class of coordination compounds.

The calculations showed that **HL^0** exists as four stable isomers (**Fig. S10**). Two major isomers are (*E*) and (*Z*), depending on the conformation of the azomethine group, and each of them, depending on the position of the N atom, can be "open" and "closed," potentially acting as bi- or tridentate ligands. Relative energies of the molecules calculated *in vacuo* suggest that the only significant isomers are the (*E*) ones. Therefore, the rest of the calculations were performed only for these. In all cases, for the free ligands (**HL^0**, **HL^1** and **HL^2**) the more stable isomers are the "open" ones with the energy differences varying from 4.5 (*in vacuo*) to 2.3 kcal/mol (water) for **HL^0** (**Table S6**) with the energy barrier from 7.2 (*in vacuo*) to 5.9 kcal/mol (water). The energy difference between "open" and "closed" isomers of **HL^1** and **HL^2** are very similar to the difference found for **HL^0** (**Table S6**). Deprotonation of **HL^0** does not change the preferred

orientation, giving the energy difference in the 8.1 – 1.4 kcal/mol range. However, the formation of the **KL^0** complex reverses the order with the “closed” isomer more stable by 7.6 – 1.7 kcal/mol. Surprisingly, for the **ZnL^{0}Cl** complex (**Fig. 6 - A**) the “closed” isomer is more stable only by 0.3 – 2.2 kcal/mol (**Fig. 6 - B**, **Table S6**), with the biggest difference being found in the most polar environment. Moreover, such small difference suggests that both isomers can be formed and coexist in a large population of molecules.

To verify the possibility of dynamic properties leading to the reorganization of the isomers, we checked a rotational energy barrier by partially optimizing the structures with the torsion angle θ, fixed to a set of different values from 0 to 180° (**Fig. 6 – A**). The results obtained from the calculation in different environments are presented in **Figure 6 - C**. They show that the energies of the conformers characterized by θ = 90°, which correspond to the energy barriers of the transition from “closed” to “open”, are only 6.73, 6.92, 7.61, and 7.62 kcal/mol, respectively, *in vacuo*, in *n*-hexane, DMSO and water.

Regarding the **Zn(L^0)$_2$** complex, there are three stable isomers (**Fig. 6 - E**): the lowest energy **Zn(L^0)$_2$-cc** with $\theta_1 \approx 0°$ and $\theta_2 \approx 0°$, **Zn(L^0)$_2$-co** with $\theta_1 \approx 0°$ and $\theta_2 \approx 160°$ and **Zn(L^0)$_2$-co** with $\theta_1 \approx 160°$ and $\theta_2 \approx 160°$. The energy difference between **Zn(L^0)$_2$-cc** and **Zn(L^0)$_2$-co** is in the range from 1.7 kcal/mol *in vacuo* to 2.8 kcal/mol in water, and the energy difference between **Zn(L^0)$_2$-co** and **Zn(L^0)$_2$-oo** is much smaller: from 0.9 kcal/mol *in vacuo* to 1.4 kcal/mol in water (**Fig. 6 - D**, **Table S7**). Due to higher computational costs, the conformational analysis was performed only *in vacuo*. The results (**Fig. 6 - G**) show that the rotational barriers between **Zn(L^0)$_2$-cc** and **Zn(L^0)$_2$-co** depend on the route and are 6.24 kcal/mol for $\theta_2 = 90°$ and 7.97 kcal/mol for $\theta_2 = 270°$. Analogously, the rotational between **Zn(L^0)$_2$-co** and **Zn(L^0)$_2$-oo** are 5.82 kcal/mol for $\theta_2 = 90°$ and 7.24 kcal/mol for $\theta_2 = 270°$. Notably, the lower values do not exceed the energy barrier for **ZnL^{0}Cl**.

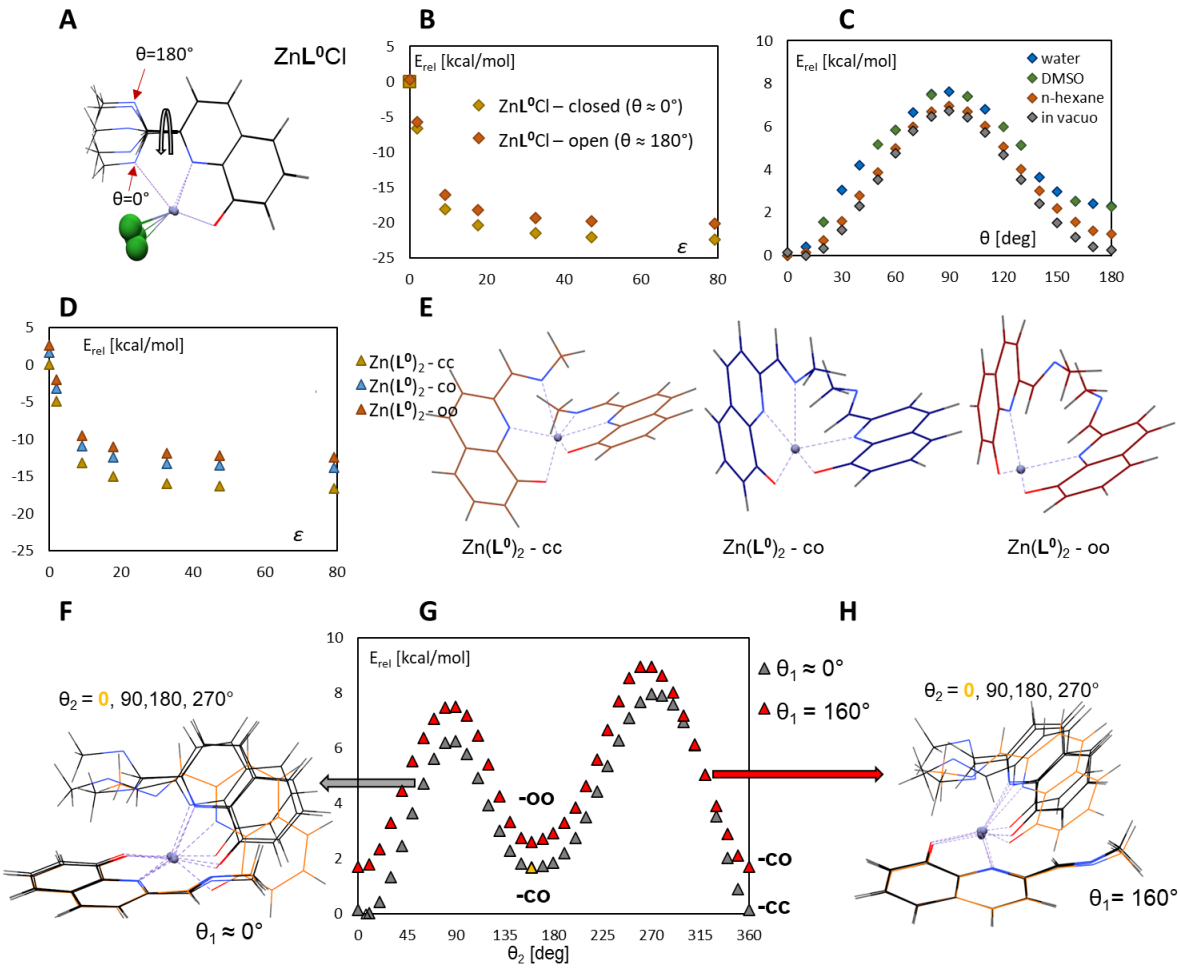

Figure 6. Analyzed isomers of **ZnL^{0}Cl** (A-C) and **Zn(L^0)$_2$** (D-H). **A**: the structures of different conformers of **ZnL^{0}Cl**; **B**: relative energies of the "open" and "closed" isomers of **ZnL^{0}Cl** in different environments; **C**: relative energies of **ZnL^{0}Cl** optimized with fixed values of θ in the 0 – 180° range; **D**: relative energies of the of **-cc**, **-co** and **-oo** isomers of **Zn(L^0)$_2$** in different environments; **E**: structures of **-cc**, **-co** and **-oo** isomers of **Zn(L^0)$_2$**; **F**: the structures of different conformers of of **Zn(L^0)$_2$** with $\theta_1 \approx 0°$ and θ_2 = 0, 90, 180 and 270°; **G**: relative energies of **Zn(L^0)$_2$** optimized with $\theta_1 \approx 0°$ and fixed values of θ_2 in the 0 – 360° range (grey triangles) and relative energies of **Zn(L^0)$_2$** optimized with θ_1 = 160° and fixed values of θ_2 in the 0 – 360° range (red triangles); **H**: the structures of different conformers of **Zn(L^0)$_2$** with θ_1 = 160° and θ_2 = 0, 90, 180 and 270°.

Interestingly, the structure of **Zn(L^0)$_2$-oo** (**Fig. 6 - E**) is not square-planar in contrast to the X-ray structure of **[Zn(L^1)$_2$]$_n$**, showing rather small torsion angle between the planes of the aromatic rings, being 60.5° *in vacuo* and suggesting the coordination of the additional ligands in the *cis* mode. This prompted us to test the possibility of the formation of the square-planar complex through conformational changes. Since the definition and modification of torsional angles between the planes is not possible with our software, we tentatively defined it as Γ– the torsion angle between C8-O1 bonds (for the atoms numeration, see **Scheme 1**). Results summarized in **Fig. S11** show that for free **Zn(L^0)$_2$** complex, the relative energy of the flattened

conformation is higher only by 5.2 kcal/mol, which suggests strong dynamics of this complex in solution. The presence of one coordinated molecule of water does not facilitate the process, and the energy difference is slightly higher: 6.1 kcal/mol. However, coordination of one molecule of DMSO or 1-methyl-1*H*-imidazole completely changes the picture – flattening of the structure becomes favourable, with a very low energy barrier (1.8 or 1.2 kcal/mol) between the flattened and typical conformations.

To summarize, we have shown that **HL^0**, and most likely also **HL^1** and **HL^2**, can act as a tri- or bidentate ligands with low energy differences between these two modes. Also, the energy barriers do not exceed 8 kcal/mol (0.35 eV, 33.5 kJ/mol), and are comparable to the Gibbs energy values for the barriers in analogous isomerization of the neutral N'-((8-hydroxyquinolin-2-yl)methylene)benzohydrazides [12]. This strongly suggests the possibility of a dynamic behaviour of the **$Zn(L^1)_2$** and **$Zn(L^2)_2$** complexes in solution.

2.6. Stability studies by UV-Vis

Before conducting biological assessments, it is crucial to evaluate the stability of compounds in solution, especially in aqueous media at physiological pH. This evaluation ensures that the complexes do not precipitate in water and remain stable against hydrolysis and decomposition throughout the duration of the studies. To determine stability, UV-vis spectroscopic measurements were performed on both the free ligands and complexes under various solvent conditions for a period of 24 h and at room temperature.

It is commonly known that Schiff bases may undergo hydrolysis in an aqueous environment [24]. Therefore, the spectral changes of **HL^1** and **HL^2** in 5% DMSO/HEPES (v/v) solution were followed with time. **Figure S12** shows that the ligands precipitate with time, and this effect is especially visible for the intraligand $n \rightarrow \pi^*$ transitions of the azomethine group.

The Zn(II)-complexes show the same behaviour as the ligands in aqueous solution, i.e., a precipitation over time that is accompanied by the formation of isosbestic points. Moreover, the disappearance of the charge transfer band (at *ca.* 465 nm) is evident, showing loss of their chemical integrity (**Figures S13 and S14**).

Bovine serum albumin (BSA) is frequently used as a substitute for human serum albumin (HSA) in the study of the interactions between bioactive compounds and proteins given its cost-effectiveness, availability, and similarity to HSA. Additionally, the cell media used in viability assays contains micromolar amounts of BSA (added in fetal bovine serum to ensure cell growth) and this protein can bind metal complexes [25, 26]. Therefore, studying the binding of bioactive compounds to BSA is important for understanding their pharmacological effects since the formation of albumin-drug adducts can enhance the solubility and bioavailability of certain drugs.

To assess the stability of the Zn(II)-complexes in this medium, equimolar solutions of **$Zn(L^1)_2$** or **$Zn(L^2)_2$** and BSA were prepared and monitored over time using UV-vis spectroscopy. The

spectra measured upon mixing and after 1 h are different showing a decrease in absorption of the band centred at *ca.* 460 nm (**Figures S15 and S16**) but in the next 24 h only very small spectral changes are observed: a small increase of this band and isosbestic points, indicating probably an equilibrium between the free Zn complex and Zn complex:BSA adducts. The gradual increase in absorbance over the 24-hour period suggests that this equilibrium is slow, as it was previously observed for related compounds [10] and as shown by circular dichroism below. These assays indicate that in cell media, where BSA is present in a relatively high concentration [25, 27] the Zn-complexes will be stable and probably bound to this protein.

2.7. Binding to BSA - Circular Dichroism and molecular docking

Given that the Zn(II)-complexes lack optical activity and BSA does not exhibit absorption bands in the visible range, the observation of induced circular dichroism (CD) bands for mixtures of both serves as compelling evidence for the binding of the complexes in close proximity to the chiral moieties of BSA.

Experiments to evaluate the binding of the complexes to BSA were first carried out with a fixed concentration of BSA (10 μM) while gradually adding equivalents of the Zn(II)-complexes. **Figures S17** and **S18** show the CD spectra measured for solutions containing BSA:compound molar ratios of 1:0.35, 1:0.7, 1:1, 1:1.5, 1:2 and 1:2.5. This preliminary experiment was particularly useful for identifying the optimal ratio, specifically a 1:2 ratio, where the CD signal remained stable above that concentration threshold, at 24 h.

The variation of the circular dichroism spectra of BSA−Zn(II) complexes solutions with time (**Fig. 7**) shows the appearance of induced CD bands due to the interaction. While the spectrum at time zero is weak and presents bands at 287 (+) and 270 (−) nm, different bands develop after 1 h, with maxima at 284 (+) and 303 (−) nm, whose intensity increases with time, as well as an isosbestic point at 296 nm. This effect can also be observed in the HT spectra, which is related to the radiation reaching the CD detector, and is analogous to an absorption spectrum and that also shows an isosbestic point (**Fig. S19**). Similar results were obtained for our previously reported Zn(II)-compounds [10]. Moreover, under the same conditions, the free ligands alone (**Fig. S20**) or $ZnCl_2$ [10] (both in the presence of BSA) do not show CD bands, even after 24 h.

These spectroscopic assays clearly show that the Zn-complexes bind BSA in a slow process and that possibly two different binding sites are available in the protein.

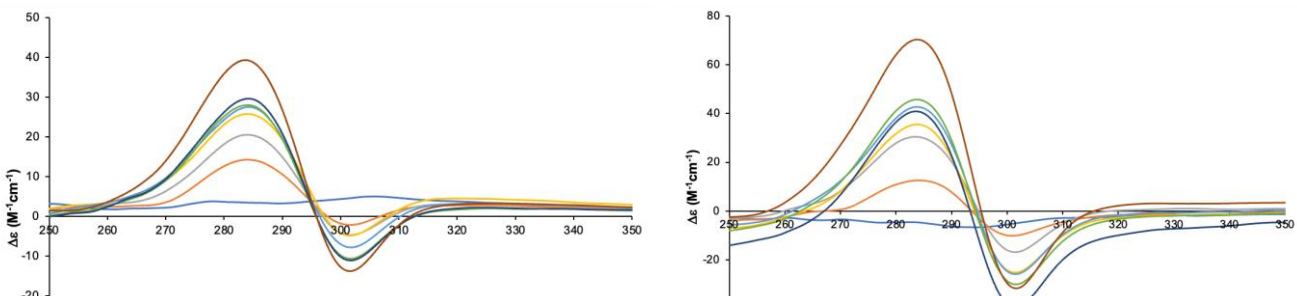

$Zn(L^1)_2$ **$Zn(L^2)_2$**

Figure 7. CD spectra of solutions containing BSA (10 μM) and **$Zn(L^1)_2$** or **$Zn(L^2)_2$** (1:2) measured with time (indicated in hours in the legend).

Molecular docking to 4OR0 BSA molecule [28] was performed to get further insight into the compounds' binding to this albumin. Three types of experiments were performed: blind docking within a large box covering the whole albumin molecule and two specific dockings centred at C(α) atom of Trp134 and Trp213 residues (box size: 25x25x25 or 30x30x30 $Å^3$). Results are presented in **Fig. 8** and **Table S8**. Analysis of the combined results shows that the preferred binding site for the **HL^1** and **HL^2** ligands is Drug Site 1 (DS1), in close proximity to the Trp213 residue. Binding energies comparable with the energies for warfarin suggest a strong binding. The second possible binding site is Fatty Acid site 6 (FA6) close to Trp134. However, much lower binding energies indicate that binding in this site is less probable. The **$Zn(L^1)_2$** and **$Zn(L^2)_2$** complexes preferably bind in the cleft between subdomains IB and IIIA with the shortest distances from the molecules to Trp134 and Trp213 around 15 Å. Binding in a close vicinity of Trp213 is much less probable, most likely due to their relatively large volume. Interestingly, binding energies for the ligands and complexes do not differ significantly. This suggests that induced chirality observed only for the complexes in the presence of BSA may be a result of the formation of a coordination bond between Zn(II) atom and the albumin. Considering the substantial flexibility of the complexes, such a scenario cannot be ruled out.

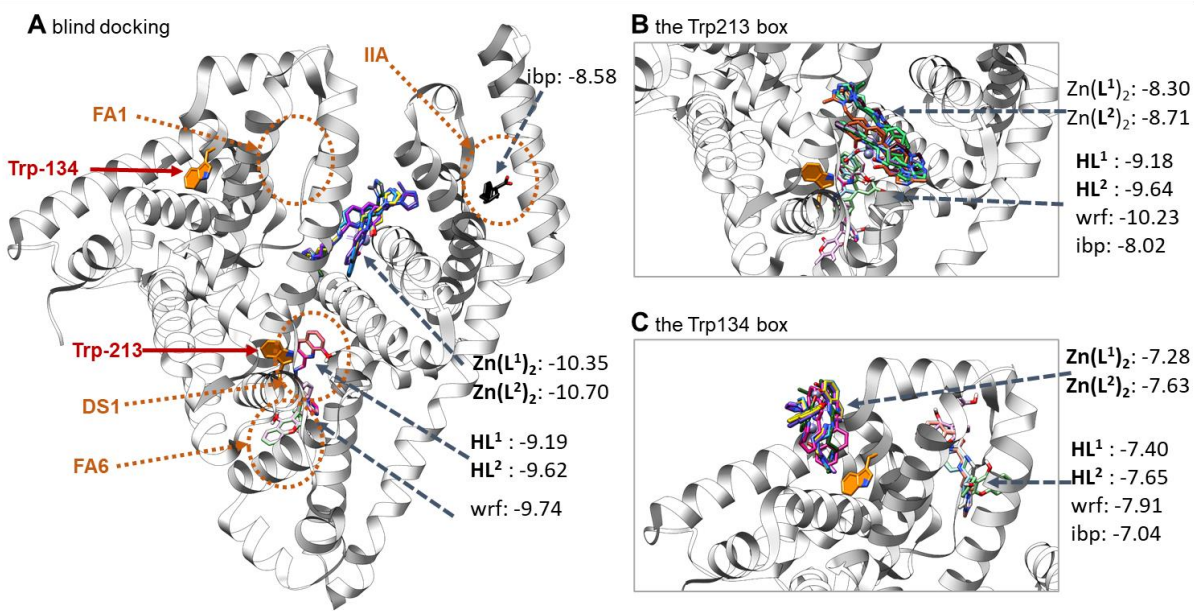

Figure 8. Molecular docking (Vina 1.2.3) to 4OR0 BSA molecule. **A:** General view of the albumin molecule with results from the blind docking together with the binding energies [kcal/mol] of lowest energy isomers) **B:** Lowest energy isomers from the Trp213-centred docking **C:** Lowest energy isomers from the Trp134-centred docking. (wrf: *R*- or *S*-warfarin; ibp – ibuprofen)

2.8. In vitro DNA binding assay

To determine whether the ligands and Zn(II)-complexes could directly interact with or induce alterations in DNA, pure plasmid DNA was incubated with the compounds and subjected to agarose gel electrophoresis to observe potential differences in migration patterns. Established DNA-damaging agents such as doxorubicin, temozolomide, and cisplatin were employed as controls. As anticipated, cisplatin intercalated with DNA, prompting further coiling and consequently faster migration. Doxorubicin induced DNA double-strand breaks, evident from the loss of both supercoiled and nicked plasmid DNA bands. Conversely, temozolomide had no discernible effect on migration. Similarly, neither the ligands nor the Zn(II)-complexes impacted migration. The addition of NaN_3, a well-known reactive oxygen species scavenger, reversed all cisplatin-induced effects, yet no alterations were observed when co-incubated with the complexes, doxorubucin or temozolomide (**Fig. S21**).

Thus, the DNA binding capabilities of the Zn(II)-complexes appear to require the presence of additional molecules to elicit any effect, and the *in vitro* conditions, which are depleted of any cytosolic salts and proteins, do not seem to reflect cellular conditions.

2.9. Biological Studies

2.9.1. Assessment of cytotoxicity

To evaluate the anticancer potential of these compounds, their cytotoxic effects were accessed across a range of cell lines originating from different sources, with a particular focus on human

breast cancer cells (MDA-MB-231, MDA-MB-453, MCF7, BT549), as well as prostate (Du145), pancreas (Panc-1), lung (A549), and melanoma (A375) cell lines, comparing them to control cells (RPE-1 cells). The IC_{50} values are given in **Table 1** and dose-response curves are depicted in **Fig. S22.** As anticipated, **HL^1** and **HL^2** showed no cytotoxic effects or lower effects than their corresponding Zn(II)-complexes, which demonstrated heightened efficacy across all tested cancer cell lines, with the exception of A549 cells, which showed resistance to all drugs, except cisplatin (**Fig. S22**). The consistent cytotoxic response observed in other cancer cell lines suggests that rather than being specific to lung cancer, the resistance of A549 cells likely stems from genetic variations enabling them to better mitigate Zn-induced damage. In comparison, the positive control cisplatin exhibited greater effectiveness than the Zn(II)-complexes in most cancer cells, albeit causing significant damage to normal control cells akin to its impact on cancer cells. In contrast, the Zn(II)-complexes demonstrated efficient cancer cell eradication while sparing normal cells, suggesting a promising therapeutic window for these compounds. Moreover, their IC_{50} values are comparable to cisplatin in the triple-negative MDA-MB breast cancer cells.

Table 1. IC_{50} values of compounds **$Zn(L^1)_2$**, **$Zn(L^2)_2$**, **HL^2**, **HL^1** and cisplatin (μM ± SD) on RPE-1, MDA-MB-231, MDA-MB-453, MCF-7, BT549, Du145, Panc-1, A549 and A375 cell lines, at 72 h incubation.

IC_{50} Table									
	RPE-1	**MDA-MB-231**	**MDA-MB-453**	**MCF-7**	**BT549**	**Du145**	**Panc-1**	**A549**	**A375**
$Zn(L^1)_2$	>50	13.04 ± 3.4	12.27 ± 0.1	7.31 ± 2.4	10.07 ± 2.3	18.24 ± 7.0	32.36 ± 16.3	>50	6.13 ± 0.5
$Zn(L^2)_2$	>50	14.64 ± 5.7	16.59 ± 1.7	6.64 ± 1.0	11.30 ± 2.7	21.58 ± 6.8	34.69 ± 16.1	>50	6.9 ± 1.0
HL^2	>50	36.97 ± 6.5	>50	18.16 ± 6.7	36.73 ± 4.8	>50	>50	>50	22.59 ± 1.2
HL^1	>50	38.26 ± 21.4	>50	18.45 ± 8.6	36.39 ± 7.6	50.21 ± 1.1	>50	>50	21.96 ± 0.1
Cisplatin	4.76 ± 2.1	13.43 ± 5.6	12.42 ± 4.6	4.96 ± 0.4	2.09 ± 1.4	2.36 ± 0.1	9.87 ± 1.9	2.6 ± 1.1	4.72 ± 4.0

When compared to the previously reported Zn(II)-complexes containing morpholine and piperidine, which were tested in A375 melanoma cancer cells, their cytotoxicity is probably similar, since higher IC_{50} values were obtained for those but at a lower incubation time (after 48 h) [10]. However, the imidazole derived complexes have much higher selectivity, particularly towards melanoma cells.

2.9.2. Assessment of apoptosis

Acridine orange and ethidium bromide (AO/EB) staining were used to observe nuclear changes and apoptotic body formation, key markers of apoptosis. With this method, both live and dead cells are stained with acridine orange, while ethidium bromide specifically labels late apoptotic or dead cells with compromised membranes. Live cells appear green, early apoptotic cells show bright green dots in irregular nuclear structures, and late apoptotic cells appear

orange/red with condensed or fragmented nuclei. Although necrotic cells also appear red, their nuclear structure resembles that of viable cells.

Compared to control cells, treatment of MDA-MB-231 cells with the Zn(II)-complexes increased both the intensity of AO and also the number of EB-positive cells (**Fig. 9**). They also displayed nuclear morphology typical of apoptotic cells, such as fragmentation and condensation (**insets in Fig. 9**). Hence, the cytotoxic effect induced by the Zn(II)-complexes appeared to be through the induction of apoptotic pathways.

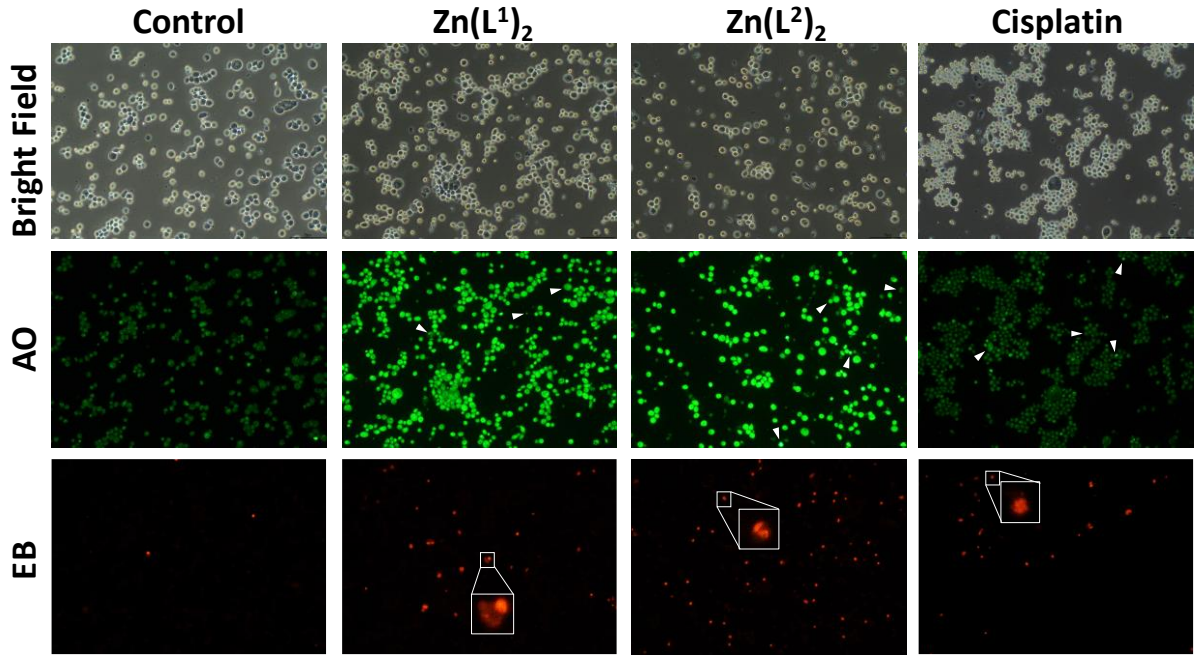

Figure 9. Induction of apoptosis upon treatment with the indicated complexes. MDA-MB-231 cells were treated with **$Zn(L^1)_2$**, **$Zn(L^2)_2$** or cisplatin and assessed for induced apoptosis via acridine orange/ethidium bromide (AO/EB) staining. The stained cells were visualized using fluorescent microscopy. Arrowheads highlight cells exhibiting brighter staining with AO, with apoptotic morphology. Insets in the ethidium bromide staining display cells in the late apoptotic/dead state.

Given the indication of apoptosis by AO/EB staining, we aimed to quantitatively determine the mode of cell death. A375 and MDA-MB-231 cells were exposed to the Zn(II)-complexes and cisplatin, and apoptosis induction was evaluated through Annexin-V staining (**Fig. 10**) and caspase 3/7 activation (**Fig. 11**) using flow cytometry. Results from these assays, based on different mechanisms - Annexin-V detecting membrane asymmetry and the induction of critical proteases for cellular protein cleavage - revealed a substantial rise in both early and late apoptosis populations when compared to the untreated (NT) group (**Fig. 10B, Fig. 11B**). While all compounds demonstrated similar levels of cytotoxicity (**Fig. S22** and **Table 1**), overall, the zinc complexes exhibited greater induction of apoptosis, compared to cisplatin, in triple-negative MDA-MB-231 cells, while showing slightly reduced efficacy in A375 cells. The

observed differences in apoptosis levels and cytotoxic response suggest alternative pathways activated by the complexes, despite apoptosis being their primary mechanism. The difference in experimental conditions, specifically the extended duration of exposure to the compounds for cytotoxicity assessment (72 h), as opposed to the shorter duration used for apoptotic measurements (48 h), may have also played a role. These collective findings imply that the cytotoxic effect may not solely depend on apoptosis; rather, some of the decrease in cell viability could be attributed to slowed cell division or cell cycle arrest induced by these complexes.

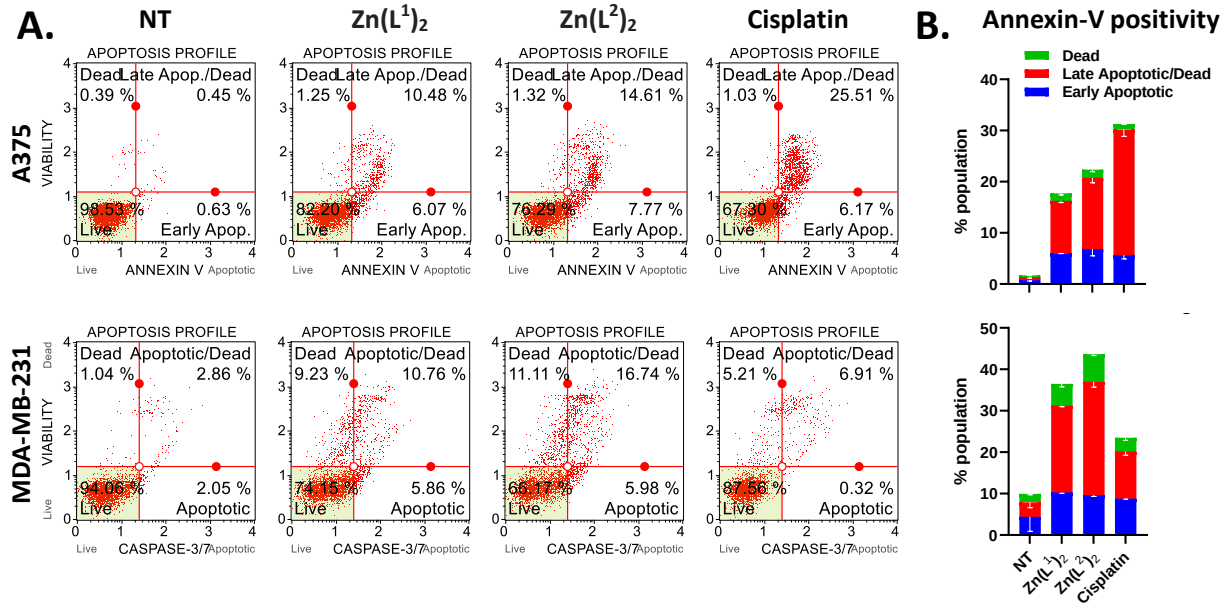

Figure 10 – Apoptosis induction was examined following treatment with the specified compounds. (**A**) Annexin V/7-AAD positivity in A375 (top panel) and MDA-MB-231 cells (bottom panel) was analyzed using flow cytometry. (**B**) Quantification of the results was performed, with error bars indicating the standard deviation from the mean. Each experiment involved scoring 5000 cells. Cells were exposed to **$Zn(L^1)_2$**, **$Zn(L^2)_2$**, or cisplatin at half inhibitory concentrations for 48 hours and assessed using the Muse Cell Analyzer. (NT: Not treated, DMSO alone control).

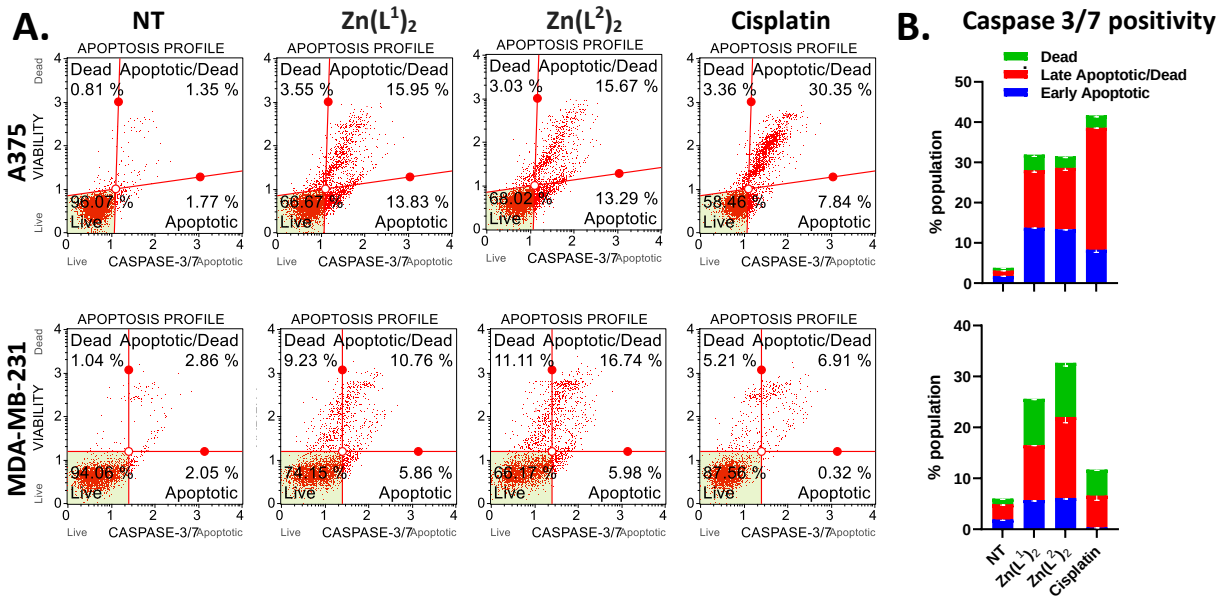

Figure 11. Apoptosis induction was assessed after administering the indicated compounds. (**A**) Flow cytometry was utilized to analyze caspase3/7 positivity in A375 (top panel) and MDA-MB-231 cells (bottom panel). (**B**) The results were quantified, with error bars representing the standard deviation from the mean. Each experiment entailed scoring 5000 cells. Cells were treated with **Zn(L^1)$_2$**, **Zn(L^2)$_2$**, or cisplatin at half inhibitory concentrations for 48 hours and examined using the Muse Cell Analyzer.

2.9.3. Induction of Oxidative Stress and DNA Damage

Given that many metal-based drugs function by inducing oxidative stress and DNA damage, our aim was to determine if treatment with the Zn(II)-complexes would lead to an increase in reactive oxygen species (ROS) levels. We assessed ROS using dihydroethidium (DHE), which undergoes oxidation upon reacting with superoxide anions, resulting in red fluorescence. A375 and MDA-MB-231 cells were treated with either the Zn(II)-complexes or cisplatin, and ROS levels were measured using a flow cytometer (**Fig. 12A**). Both **Zn(L^1)$_2$** and **Zn(L^2)$_2$** effectively increased ROS in both cell lines (**Fig. 12B**). Similarly to apoptosis levels, ROS induction by the complexes was higher in MDA-MB-231 cells, compared to A375 cells, and even higher than that of cisplatin.

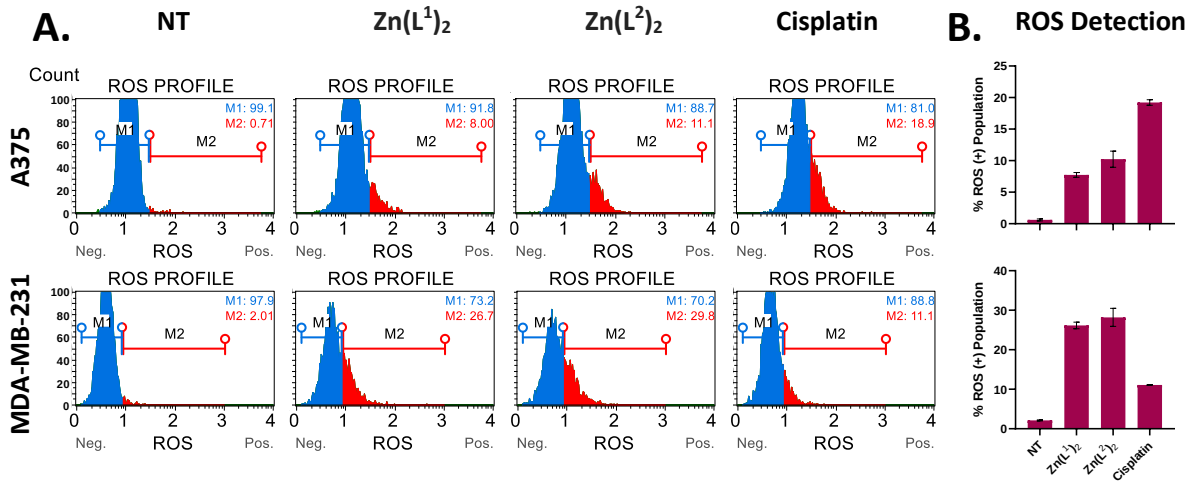

Figure 12. Induction of oxidative stress was evaluated following treatment with indicated complexes. (**A**) A-375 (top panel) and MDA-MB-231 (bottom panel) cells were exposed to **$Zn(L^1)_2$, $Zn(L^2)_2$** or cisplatin and examined for ROS activation using dihydroethidium staining. Representative flow diagrams are depicted. (**B**) Quantification of the experiments was performed by determining the percentage of the population falling within the M2 region in (A). The error bars show the standard deviation from the mean. Cell scoring was conducted using the Muse Cell Analyzer. (NT: Not treated, DMSO alone control).

To determine whether the complexes or the elevated ROS levels led to DNA damage, we focused on the formation of DNA double-strand breaks (DSBs), which are highly detrimental. As expected, there was a significant increase in the number of DNA breaks following drug exposure (**Fig. 13A**). Cisplatin induced significantly more DSBs compared to both complexes (**Fig. 13B**), affecting over 80% of the cells, despite inducing similar levels of ROS and apoptosis. This, in fact, provides a base for the notion that complexes of endogenous metal ions are less toxic and potentially have fewer side effects. Nevertheless, compared to normal cells, they remain effective in selectively killing cancer cells.

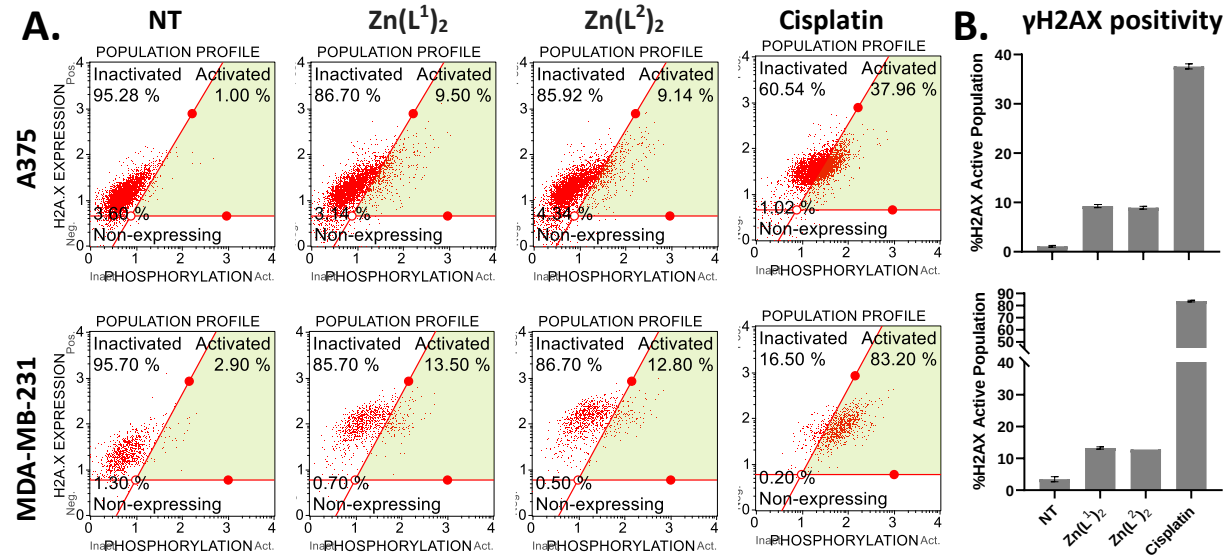

Figure 13. Induction of DNA double-strand breaks was investigated upon treatment with the compounds. (**A**) A-375 (top) and MDA-MB-231 cells (bottom) were subjected to staining with antiphospho-Histone H2A.X (Ser139), Alexa Fluor® 555, and anti-Histone H2A.X, PECy5-conjugated antibodies subsequent to treatment with **$Zn(L^1)_2$**, **$Zn(L^2)_2$** or cisplatin. (**B**) Quantitative analysis of experiments conducted in the activated panel depicted in olive green. Standard deviation from the mean is represented by the error bars. Cell scoring was performed using the Muse Cell Analyzer. (NT: Not treated, DMSO alone control).

3. CONCLUSIONS

Two new Schiff bases derived from nitrogen-based heterocycles (8-hydroxyquinoline and imidazole) as well as their Zn(II)-complexes were designed, prepared and characterized in solution and solid state. Interestingly, in the solid state a polymeric 1D structure was obtained for **$Zn(L^1)_2$** in which octahedral coordination geometry was achieved through binding of the imidazole nitrogens to neighbouring molecules. In solution these polymers are probably destroyed, and monomeric complexes are formed, since the DFT calculations showed a dynamic behaviour for this type of Zn-complexes.

The complexes show limited stability in aqueous media, which increases upon binding to BSA. Spectroscopic and theoretical docking studies, indicate strong binding to albumin, which may impact their pharmacokinetic properties.

Overall, the Zn(II)-complexes exhibited a less pronounced impact on cell viability, when compared to the clinically utilized positive control cisplatin, except in triple-negative breast cancer cells in which they are comparable. However, they displayed higher selectivity towards cancer cells relative to normal counterparts. As anticipated, the ligands alone demonstrated low or no cytotoxicity, even at elevated concentrations, suggesting that the observed cytotoxicity was attributed to the metal complex. Like other metal-based agents, both Zn(II)-complexes effectively induced reactive oxygen species and DNA double-strand breaks. However, this effect was not observed in cell-free systems, indicating the necessity of cytosolic molecules for exerting any cytotoxic effect. Since Zn(II) has no redox activity, this is not a surprise.

Apoptosis was identified as the primary mode of cell death through AO/EB and Annexin-V/7AAD staining, and caspase 3/7 activity assays. Compared to our previously described Zn(II)-complexes [10], the efficacy of the compounds presented herein demonstrated improved induction of apoptosis in A375 cells (~15% versus ~30%). Since apoptosis does not elicit inflammatory responses like necrosis, it is considered the preferred pathway for clinical drug use. Hence, the Zn(II)-complexes exhibit promise for their semi-selectivity towards cancer cells and their mechanism of inducing cell death, making them potential candidates for clinical application.

4. EXPERIMENTAL SECTION

All common laboratory chemicals were purchased from commercial sources and used without further purification. Synthesized compounds were characterized by C, H and N elemental analyses, ESI-MS and by UV-Vis, FTIR, ^{1}H NMR/^{13}C NMR spectroscopies.

4.1. Materials and methods

The chemicals 8-hydroxy-2-quinoline carbaldehyde, 1-(3-aminopropyl)imidazole and 1-(3-aminopropyl)2-methyl-1H-imidazole were purchased from Aldrich and used as received. HEPES (4-(2-hydroxy ethyl)-1-piperazine ethane sulfonic acid) was obtained from Sigma. $ZnCl_2$ was purchased from Thermo Scientific. The water used in all biological studies was double-deionized in a Milli-Q (MQ) system (Millipore). All the remaining chemicals used were of analytical grade.

^{1}H and ^{13}C NMR spectra were recorded at ambient temperature on a Bruker Avance + 400 MHz spectrometer. ^{1}H and ^{13}C chemical shifts (δ) are expressed in ppm relative to the deuterated solvent residual peak. Electronic UV-Vis absorption spectra were recorded with a Perkin Elmer Lambda 35 spectrophotometer. Infrared spectra (IR, 4000–400 cm^{-1}) were recorded on a Jasco FT/IR 4100 spectrophotometer in KBr pellets. Elemental analysis for C, H and N, were carried out on a FISONS EA 1108 CHNS-O apparatus at *Laboratório de Análises* of *Instituto Superior Técnico*. A LCQ FleetTM Ion Trap Mass Spectrometer from Thermo Scientific was used to measure ESI-MS spectra of methanolic solutions of the compounds in both the positive and negative ion modes.

4.2. Synthesis and characterization of the ligand precursors

To a methanolic solution of the selected amine (1 mmol) and KOH (1 mmol), 8-hydroxy-2-quinolinecarboxaldehyde (1 mmol) was added. The resulting orange solution was stirred for 1 h at room temperature. After completion, the solution was evaporated and the oily residue was dissolved in dichloromethane, filtered, evaporated and redissolved in acetone, and recrystallized with diethyl ether.

HL^{1}: Yield: 87%. Orange foam. ^{1}H NMR [DMSO-d_6, Me_4Si, δ/ppm]: 8.43 [s, 1, H_{11}]; 7.94 [d, 1, $^{3}J_{HH}$ = 8, H_4]; 7.72 [d, 1, $^{3}J_{HH}$ = 8, H_3]; 7.63 [s, 1, H_{15}]; 7.18 [s, 1, H_{17}]; 7.14 [t, 1, $^{3}J_{HH}$ = 8, H_6]; 6.89 [s, 1, H_{16}]; 6.47 [d, 2, $^{3}J_{HH}$ = 8, H_5+H_7]; 4.00 [t, 2, $^{3}J_{HH}$ = 8, H_{14}], 3.46 [t, 2, $^{3}J_{HH}$ = 8, H_{12}], 2.00 [m, 2, H_{13}]. ^{13}C NMR [DMSO-d_6, Me_4Si, δ /ppm]: 168.67 (C_8); 164.02 (C_{11}); 148.00 (C_2); 143.75 (C_9); 137.32 (C_{15}); 135.61 (C_4); 131.60 (C_{10}); 130.44 (C_6); 128.44 (C_{16}); 119.36 (C_{17}); 117.12 (C_3); 114.09 (C_7); 104.91 (C_5); 57.00 (C_{12}); 44.17 (C_{14}); 31.95 (C_{13}). UV-Vis: [DMSO, λ_{max}/nm (ε/$M^{-1}cm^{-1}$)]: 315 (sh), 351 (1946); IR [KBr, cm^{-1}]: 3402 (ν_{O-H}); 2942 (ν_{C-H} aliphatic); 1644 ($\nu_{C=N}$); 1541 ($\nu_{C=C}$ aromatic); 1510 (ν_{C-C} aromatic); 1090 (ν_{C-O}); Elemental analysis calc.

for $C_{16}H_{15}N_4OK$•1.1 H_2O (336.10 g/mol): C: 56.82, H: 5.13, N: 16.56. Found: C: 56.40, H: 4.43, N: 16.26; Mass spectrometry MS (ES^+): m/z (calcd): 281.14, found: 281.18 [$M+H^+$].

HL^2: Yield: 81%. Orange foam. ^1H NMR [DMSO-d_6, Me_4Si, δ/ppm]: 8.50 [s, 1, H_{11}]; 8.14 [d, 1, $^3J_{HH}$ = 8, H_4]; 7.90 [d, 1, $^3J_{HH}$ = 12, H_3]; 7.29 [t, 1, $^3J_{HH}$ = 8, H_6]; 7.08 [s, 1, H_{15}]; 6.94 [d, 1, $^3J_{HH}$ = 8, H_5]; 6.89 [d, 1, $^3J_{HH}$ = 8, H_7]; 6.73 [s, 1, H_{16}]; 3.97 [t, 1, $^3J_{HH}$ = 8, H_{14}]; 3.57 [t, 1, $^3J_{HH}$ = 8, H_{12}]; 2.28 [s, 1, H_{18}]; 2.02 [t, 1, $^3J_{HH}$ = 8, H_{13}]. ^{13}C NMR [DMSO-d_6, Me_4Si, δ /ppm]: 163.51 (C_{11}); 161.57 (C_8); 150.24 (C_2); 143.80 (C_{17}); 141.06 (C_9); 136.22 (C_4); 130.50 (C_{10}); 129.55 (C_6); 126.35 (C_{16}); 119.57 (C_{15}); 117.47 (C_3); 113.33 (C_7); 111.47 (C_5); 57.02 (C_{12}); 43.20 (C_{14}); 31.61 (C_{13}); 12.67 (C_{18}); UV-Vis: [DMSO, λ_{max}/nm (ε/$M^{-1}cm^{-1}$)]: 314 (sh), 351 (1872); IR [KBr, cm^{-1}]: 3420 (ν_{O-H}); 2933 (ν_{C-H} aliphatic); 1646 ($\nu_{C=N}$); 1541 ($\nu_{C=C}$ aromatic); 1504 (ν_{C-C} aromatic); 1092 (ν_{C-O}); Elemental analysis calc. for $C_{17}H_{17}N_4OK$•0.9 H_2O (494.20 g/mol): C: 58.56, H: 5.43, N: 16.07. Found: C: 58.60, H: 5.43, N: 15.87; Mass spectrometry MS (ES^+): m/z (calcd): 295.16, found: 295.20 [$M+H^+$].

4.3. Synthesis and characterization of the complexes

To an ethanolic solution of the adequate amine (2 mmol) and KOH (2 mmol), 8-hydroxy-2-quinolinecarboxaldehyde (2 mmol) was added. The resulting orange solution was stirred for 1 h at room temperature. $ZnCl_2$ (1 mmol), was then added and the resulting solution was stirred at room temperature for 1 h and subsequently evaporated. The precipitate was dissolved in dichloromethane, filtered, and recrystallized with diethyl ether.

$Zn(L^1)_2$: Yield: 55%. Dark orange powder. ^1H NMR [DMSO-d_6, Me_4Si, δ/ppm]: 8.66 [s, 2, H_{11}]; 8.46 [d, 2, $^3J_{HH}$ = 8, H_4]; 7.96 [d, 2, $^3J_{HH}$ = 8, H_3]; 7.53 [s, 2, H_{17}]; 7.40 [t, 2, $^3J_{HH}$ = 8, H_6]; 6.97 [m, 4, H_5+H_{15}]; 6.65 [m, 4, H_7+H_{16}]; 3.75 [m, 4, H_{14}]; 3.27 [m, 4, H_{12}]; 1.65 [m, 4, H_{13}]. ^{13}C NMR [DMSO-d_6, Me_4Si, δ /ppm]: 163.56 (C_8); 160.72 (C_{11}); 142.57 (C_2); 139.53 (C_9); 139.13 (C_4); 137.61 (C_{17}), 131.67 (C_6); 130.53 (C_{10}); 127.81 (C_{16}); 119.69 (C_3+C_{15}); 112.42 (C_7); 108.78 (C_5); 56.29 (C_{12}); 43.75 (C_{14}); 30.60 (C_{13}); UV-Vis: [DMSO, λ_{max}/nm (ε/$M^{-1}cm^{-1}$)]: 269 (26617); 298 (45644); 344 (sh); 367 (sh); 488 (2652). UV-Vis: [CH_2Cl_2, λ_{max}/nm (ε/$M^{-1}cm^{-1}$)]: 269 (sh); 300 (50565); 349 (sh); 371 (sh); 453 (sh); 492 (2699); IR [KBr, cm^{-1}]: 2933 (ν_{C-H} aliphatic); 1640 ($\nu_{C=N}$); 1594 ($\nu_{C=C}$ aromatic); 1502 (ν_{C-C} aromatic); 1105 (ν_{C-O}); Elemental analysis calc. for $C_{32}H_{30}N_8O_2Zn$ • 1.5 H_2O (651.05 g/mol): C: 59.04, H: 5.11, N: 17.21. Found: C: 59.49, H: 4.24, N: 16.83; Mass spectrometry MS (ES^+): m/z (calcd): 623.19, found: 623.07 [$M+H^+$].

$Zn(L^2)_2$: Yield: 51%. Light orange powder. ^1H NMR [DMSO-d_6, Me_4Si, δ/ppm]: 8.79 [s, 2, H_{11}]; 8.39 [d, 2, $^3J_{HH}$ = 8, H_4]; 7.97 [d, 2, $^3J_{HH}$ = 8, H_3]; 7.41 [t, 2, $^3J_{HH}$ = 8, H_6]; 6.99 [m, 4, H_{15}+H_5]; 6.76 [d, 2, $^3J_{HH}$ = 8, H_7]; 6.52 [s, 2, H_{16}]; 3.79 [m, 4, H_{14}]; 3.40* [m, 4, H_{12}]; 2.06 [s, 6, H_{18}]; 1.80 [m, 4, H_{13}]. ^{13}C NMR [DMSO-d_6, Me_4Si, δ /ppm]: 163.21 (C_8); 161.44 (C_{11}); 147.86 (C_2); 144.28 (C_{17}); 139.52 (C_9); 138.83 (C_4); 131.37 (C_6); 130.22 (C_{10}); 125.44 (C_{16}); 120.28 (C_{15}); 118.61

(C_3); 112.84 (C_7); 109.59 (C_5); 56.87 (C_{12}); 43.11 (C_{14}); 30.76 (C_{13}); 11.89 (C_{18}). *under the water (solvent) peak.

UV-Vis: [DMSO, λ_{max}/nm (ε/$M^{-1}cm^{-1}$)]: 268 (29125); 296 (38432); 349 (sh); 371 (sh); 468 (2044); 514 (sh). UV-Vis: [CH_2Cl_2, λ_{max}/nm (ε/$M^{-1}cm^{-1}$)]: 292 (43288); 310 (sh); 350 (sh); 372 (sh); 439 (2468); 523 (sh); IR [KBr, cm^{-1}]: 2927 (ν_{C-H} aliphatic); 1643 ($\nu_{C=N}$); 1595 ($\nu_{C=C}$ aromatic); 1502 (ν_{C-C} aromatic); 1102 (ν_{C-O}); Elemental analysis calc. for $C_{17}H_{21}N_3O$ • 2 H_2O (319.19 g/mol): C: 59.35, H: 5.57, N: 16.28. Found: C: 59.68, H: 5.32, N: 16.55; Mass spectrometry MS (ES^+): m/z (calcd): 651.22, found: 651.12 [$M+H^+$].

4.4. Single crystal X-ray diffraction

HL²: data were collected from suitable single crystals of **HL²** a Bruker D8QUEST, with graphite-monochromated radiation (Mo Kα, λ = 0.71073 Å), at 293 K. X-ray generator was operated at 50 kV and 30 mA. SHELXT 2014/4 [29] was used for structure solution and SHELXL 2014/7 [30] was used for full matrix least-squares refinement on F^2. These two programs are included in the WINGX-Version 2021.3 [31] program package. A full-matrix least-squares refinement was used for the non-hydrogen atoms with anisotropic thermal parameters. The H were inserted in idealized positions and allowed to refine in the parent atom. MERCURY 2023.3.0 [32] was used for packing diagrams. PLATON [33] was used to determine hydrogen bond interactions.

[Zn(L¹)₂]ₙ: The experimental data for the single crystals were recorded using the APEX3 software [34]. The frames were integrated with the SAINT software using a narrow-frame algorithm [35]. Data were corrected for absorption effects using the Multi-Scan method (SADABS). The structures were solved and refined using the SHELXTL Software [36].

CCDC 2335709 and 2314175 contain the supplementary crystallographic data for **HL²** and **[Zn(L¹)₂]ₙ**, respectively. These data can be obtained free of charge from The Cambridge Crystallographic Data Centre via www.ccdc.cam.ac.uk/products/csd/request/.

Table 2 summarizes the data collection and refinement details.

Table 2. Crystallographic data for **HL²** and **[Zn(L¹)₂]ₙ**.

	HL²	**[Zn(L1)₂]ₙ**
Chemical formula	$C_{34}H_{36}N_8O_2$	$C_{32}H_{30}N_8O_2Zn,2(C_2H_6OS)$
Formula weight	588.71	780.26
Crystal size (mm)	0.18 x 0.08 x 0.03	0.010x 0.060x 0.200
Crystal system	Monoclinic	Monoclinic
Space group	$P2_1/c$	$P21/c$
a (Å)	8.439(2)	9.661(17)
b (Å)	17.238(4)	8.429(17)
c (Å)	10.585(3)	22.10(4)
α (°)	90	90

β (°)	105.652(10)	92.25(4)
γ (°)	90	90
V (Å^3)	1482.7(6)	1798.(6)
Z	2	2
d (mg.cm^{-3})	1.319	1.441
μ (mm^{-1})	0.086	0.851
θ range (°)	2.321 – 26.570	27.55
Reflections collected/unique	45536 / 3039	29771
R_{int}	0.1213	0.0657
GoF	1.011	1.152
Final R indices[a,b] [$I > 2\sigma(I)$]	R_1=0.0543, wR_2 =0.1063	R_1=0.0546, wR_2 =0.1140

[a] $R_1 = \Sigma||F_o| - |F_c||/\Sigma|F_o|$; [b] $wR_2 = [\Sigma[w(F_o^2 - F_c^2)^2]/\Sigma[w(F_o^2)^2]]^{1/2}$

4.5. Stability studies by UV-Vis spectrophotometry

Stock solutions of each complex were freshly prepared in DMSO and diluted with HEPES buffer (10 mM, pH 7.4), ensuring that the organic solvent content was less than 5% (v/v). The samples were monitored by UV-Vis absorption spectrophotometry for 6 consecutive hours, and a final measurement at 24 h.

4.6. DFT Calculations and Molecular Docking

DFT calculations were performed using the Gaussian 16, Revision C.01 program [37] with ωB97XD functional from Head-Gordon and coworkers [38] which includes empirical dispersion and long-range corrections. It was shown that this functional gives usually good results in the DFT and TDDFT calculations for many types of molecules, including aromatic compounds and metal complexes [39, 40]. The basis set used was popular 6-311++G(d,p), which is compact, however gives results comparable to the ones obtained with more complex basis sets [41, 42]. All calculations were performed *in vacuo* and in several solvents (Polarizable Continuum Model (PCM) using the integral equation formalism variant (IEFPCM) [43] *n*-hexane (ε = 1.89), DCM (ε = 9.1), *n*-butanol (ε = 17.8), MeOH (ε = 32.7), DMSO (ε = 47.29), and water (ε = 79.2). Minima of the fully optimized geometries in the ground state were confirmed with the oscillation frequencies analysis.

Molecular docking experiments were performed using Autodock Vina 1.2.3 program, [44, 45], which applies a united-atom scoring function and ignores the user-supplied partial charges. Albumin macromolecule was chosen from RCSB Protein Data Bank (PDB ID 4OR0) [28]. Files for the calculations were prepared using two programs: UCSG Chimera v.1.16 [46] and AutodockTools-1.5.6 [47]. Validation of the docking method through re-docking of naproxen to 4OR0 BSA was shown in one of our previous papers [48]

4.7. Cell culturing

A-549 (ATCC, CCL-185), Du145 (ATCC, HTB-81), Panc-1 (ATCC, CRL-1469), BT-549 (ATCC, HTB-122), MDA-MB-453 (ATCC, HTB-131) and RPE-1 (ATCC, CRL-4000) cell lines were grown and cultured according to the instructions on the ATCC website. A-375 (ATCC, CRL-1619), MCF7 (ATCC, HTB-22) and MDA-MB-231 (ATCC, HTB-26) cells were grown in Dulbecco's Modified Eagle Medium with high glucose, supplemented with 10% FBS (Gibco, 10500064) and penicillin-streptomycin (10,000 U/mL, Gibco, 15140122). Cells were incubated at 37 °C, 5% CO_2 and passaged every 2–3 days.

4.8. Sulforhodamine B (SRB) assay

DMSO stock solutions (10 mM) of all compounds were prepared and stored in aliquots at −20 °C, being thawed on the day of the experiment and a single-use policy. In the SRB assay, 4 × 10^4 cells were seeded onto 96-well plates and exposed to varying concentrations of the specified compounds (0–50 μM) for 72 hours. Subsequently, trichloroacetic acid (final concentration 10%) was added to the wells and cells were fixed at 4 °C for 1 hour. Each well underwent five washes with MQ H_2O, followed by drying and incubation with 4% (v/w) SRB dye (50 μL/well) for 30 minutes at room temperature. After the incubation period, the wells were washed five times with 1% acetic acid (v/v), and 150 μL of a 10 mM TRIS-base solution was added to ensure uniform color development. Colorimetric readings were recorded at a wavelength of 564 nm. The percentage of cell viability was calculated using the formula: % Cell Viability = [100 × (Sample Abs-blank)/(Non-treated control Abs-blank)].

4.9. Agarose gel electrophoresis for compound DNA interaction assays

The procedures outlined in a previous publication were adhered to, with slight modifications [49]. In brief, plasmid DNA (200 ng, pBOS-H2B-GFP, BD Biosciences) underwent an overnight incubation at room temperature in the presence of compounds **$Zn(L^1)_2$**, **$Zn(L^2)_2$**, **HL^1**, **HL^2** and cisplatin (100–400 μM, in 20 μL). For the evaluation of ROS scavenging activity, NaN_3 (final concentration 37.5 mM in MQ H_2O) was introduced. Subsequently, the samples were electrophoresed on a 1% agarose gel (100 V, 60 minutes). The experiments were replicated twice, and the band intensities were quantified and analyzed using ImageJ software.

4.10. Flow cytometry analyses

A total of 4 × 10^4 cells were seeded onto 12-well plates. On the following day, cells were exposed to either compounds or cisplatin at concentrations of ~IC_{50}. Following a 48-hour treatment, the cells that were detached or trypsinized were suspended in a PBS solution supplemented with 1% FBS at a concentration of 10^6 cells/mL. The analyses described below were conducted following the specified protocols.

4.11. Annexin V staining

100 µL of cell suspension was mixed with Annexin V and 7-AAD solution in equal proportions, and then incubated at room temperature for 20 minutes. Cells were scored using the Muse Cell Analyzer (Merck Millipore).

4.12. Caspase 3/7 staining

A combination of 50 µL cell suspension and 5 µL Caspase 3/7 antibody (1:8 diluted in PBS) was prepared and incubated at room temperature for 30 minutes. 150 µL of the 7-AAD antibody mixture (1:75 diluted with 1 × Assay Buffer) was added to the cells and incubated at room temperature for 5 minutes. The apoptotic cells were scored using the Muse Cell Analyzer.

4.13. ɣH2AX staining

A total of 100 µL of cell suspension was mixed with 1 × fixation buffer in a 1:1 ratio and incubated on ice for 5 minutes. Subsequently, the cells underwent centrifugation (300 g, 5 minutes), and the supernatant was discarded. The resulting cell pellet was then suspended in 1 × permeabilization buffer and incubated on ice for an additional 5 minutes. After another round of washing (300 g, 5 minutes) and discarding the supernatant, the cell pellet was resuspended in a 50 µL antibody mixture. The antibodies (20×) Anti-phospho-Histone H2A.X (Ser139), Alexa Fluor 555, and (20×) Anti-H2A.X, PECy5 were appropriately diluted with 1 × assay buffer. Following a 30-minute incubation at room temperature, the cells were centrifugated and then resuspended in 200 µL of 1 × assay buffer. The analysis of double-stranded breaks was performed using the Muse Cell Analyzer.

4.14. ROS activation

The oxidative stress reagent was diluted using a 1:100 ratio of 1 × assay buffer. Subsequently, this reagent was further diluted with 1 × assay buffer at a 1:80 dilution and labeled as the oxidative stress working solution. A blend of 50 µL of cell suspension and 150 µL of the working solution was then prepared and incubated at 37 °C for 30 minutes. The Muse Cell Analyzer was used for the analysis of ROS-positive cells.

4.15. Acridine Orange/Ethidium Bromide (AO/EB) Staining

MDA-MB-231 cells were plated in 6-well plates at a density of 1.2 x 10^5 cells/well. After 48 h of treatment, both floating and attached cells were collected, centrifuged (400g, 4 min), and re-suspended in 25 µL. Following the addition of 1 µL of AO/EtBr staining solution (100 µg/mL AO and 100 µg/mL EB mixture) to the cell suspension, the samples were placed on microscope slides and covered with a coverslip. The morphology was examined using a fluorescent microscope (Eclipse TS100, Nikom), and images were captured within 20 minutes after the addition of the AO/EtBr stain.

Declaration of competing interest

The authors declare that they have no known competing financial interests or personal relationships that could have appeared to influence the work reported in this paper.

Acknowledgments

This work was partially funded by Fundação para a Ciência e a Tecnologia (FCT) through projects UIDB/00100/2020 (https://doi.org/10.54499/UIDB/00100/2020), UIDP/00100/2020 (https://doi.org/10.54499/UIDP/00100/2020), LA/P/0056/2020 (https://doi.org/10.54499/LA/P/0056/2020), and PTDC/QUI-QIN/0586/2020. The Portuguese NMR and mass spectrometry IST-UL are acknowledged for access to the equipment.

I.R. acknowledges AGAUR (Generalitat de Catalunya, projects 2017-SGR-1720) and UdG (Universitat de Girona, PONT2020/05).

This study also received support from the Koç University School of Medicine (KUSOM). CAA, BS and BY wish to express their appreciation for the utilization of the resources and amenities provided by the Koç University Research Center for Translational Medicine (KUTTAM), which is supported by the Presidency of Turkey, Head of Strategy and Budget.

The DFT calculations have been carried out in Wroclaw Centre for Networking and Supercomputing (http://www.wcss.wroc.pl), Grant No. 140. Molecular docking graphics and analyses were performed with UCSF Chimera, developed by the Resource for Biocomputing, Visualization, and Informatics at the University of California, San Francisco, with support from NIH P41-GM103311.

References

[1] A. Gomtsyan, Heterocycles in drugs and drug discovery, Chem. Heterocycl. Compd., 48 (2012) 7-10.

[2] O. Ebenezer, M.A. Jordaan, G. Carena, T. Bono, M. Shapi, J.A. Tuszynski, An Overview of the Biological Evaluation of Selected Nitrogen-Containing Heterocycle Medicinal Chemistry Compounds, Int. J. Mol. Sci., 23 (2022) 8117.

[3] E. Vitaku, D.T. Smith, J.T. Njardarson, Analysis of the Structural Diversity, Substitution Patterns, and Frequency of Nitrogen Heterocycles among U.S. FDA Approved Pharmaceuticals, J. Med. Chem., 57 (2014) 10257-10274.

[4] A. Lauria, G. La Monica, A. Bono, A. Martorana, Quinoline anticancer agents active on DNA and DNA-interacting proteins: From classical to emerging therapeutic targets, Eur. J. Med. Chem., 220 (2021) 113555.

[5] B.S. Matada, R. Pattanashettar, N.G. Yernale, A comprehensive review on the biological interest of quinoline and its derivatives, Bioorgan. Med. Chem., 32 (2021) 115973.

[6] M. Capozzi, C. De Divitiis, A. Ottaiano, C. von Arx, S. Scala, F. Tatangelo, P. Delrio, S. Tafuto, Lenvatinib, a molecule with versatile application: from preclinical evidence to future development in anti-cancer treatment, Cancer Manag. Res., 11 (2019) 3847-3860.

[7] A. Verma, S. Joshi, D. Singh, Imidazole: Having Versatile Biological Activities, J. Chem., 2013 (2013) 329412.

[8] I. Ali, M.N. Lone, H.Y. Aboul-Enein, Imidazoles as potential anticancer agents, MedChemComm, 8 (2017) 1742-1773.
[9] J. Sun, Q. Wei, Y. Zhou, J. Wang, Q. Liu, H. Xu, A systematic analysis of FDA-approved anticancer drugs, BMC Sys. Biol., 11 (2017) 87.
[10] L. Côrte-Real, V. Pósa, M. Martins, R. Colucas, N.V. May, X. Fontrodona, I. Romero, F. Mendes, C. Pinto Reis, M.M. Gaspar, J.C. Pessoa, É.A. Enyedy, I. Correia, Cu(II) and Zn(II) Complexes of New 8-Hydroxyquinoline Schiff Bases: Investigating Their Structure, Solution Speciation, and Anticancer Potential, Inorg. Chem., 62 (2023) 11466-11486.
[11] N. Ribeiro, I. Bulut, B. Sergi, V. Pósa, G. Spengler, G. Sciortino, V. André, L.P. Ferreira, T. Biver, V. Ugone, E. Garribba, J. Costa-Pessoa, É.A. Enyedy, C. Acilan, I. Correia, Promising anticancer agents based on 8-hydroxyquinoline hydrazone copper(II) complexes, Front. Chem., 11 (2023).
[12] N. Ribeiro, I. Bulut, V. Pósa, B. Sergi, G. Sciortino, J. Costa Pessoa, L.B. Maia, V. Ugone, E. Garribba, E. Enyedi, C. Acilan, I. Correia, Solution chemical properties and anticancer potential of 8-hydroxyquinoline hydrazones and their oxidovanadium(IV) complexes J. Inorg. Biochem., 235 (2022) 111932.
[13] N. Ribeiro, P.F. Farinha, J.O. Pinho, H. Luiz, J.P. Mészáros, A.M. Galvão, J. Costa Pessoa, É.A. Enyedy, C.P. Reis, I. Correia, M.M. Gaspar, Metal Coordination and Biological Screening of a Schiff Base Derived from 8-Hydroxyquinoline and Benzothiazole, Pharmaceutics, 14 (2022) 2583.
[14] N. Ribeiro, M. Albino, A. Ferreira, C. Escrevente, D.C. Barral, J.C. Pessoa, C.P. Reis, M.M. Gaspar, I. Correia, Liposomal Formulations of a New Zinc(II) Complex Exhibiting High Therapeutic Potential in a Murine Colon Cancer Model, Int. J. Mol. Sci., 23 (2022) 6728.
[15] V. Oliveri, G. Vecchio, 8-Hydroxyquinolines in medicinal chemistry: A structural perspective, Eur. J. Med. Chem., 120 (2016) 252-274.
[16] P. Ramadevi, R. Singh, A. Prajapati, S. Gupta, D. Chakraborty, Cu(II) Complexes of Isoniazid Schiff Bases: DNA/BSA Binding and Cytotoxicity Studies on A549 Cell Line, Adv. Chem., 2014 (2014) 630575.
[17] R. Diana, B. Panunzi, The Role of Zinc(II) Ion in Fluorescence Tuning of Tridentate Pincers: A Review, Molecules, 25 (2020) 4984.
[18] T. Gao, L. Meng, G. Zeng, Z. Hao, Z. Han, Q. Feng, J. Lin, Copper(II) complexes supported by 8-hydroxyquinoline-imine ligands: Synthesis, characterization and catalysis in aerobic alcohols oxidation, Polyhedron, 224 (2022) 115984.
[19] K. Nakamoto, Infrared and Raman Spectra of Inorganic and Coordination Compounds: Part A: Theory and Applications in Inorganic Chemistry, Sixth Edition, 5th ed., Wiley, 2008.
[20] R. Silverstein, F. Webster, D. Kiemle, Spectrometric Identification of Organic Compounds. 7th ed., Hoboken NJ, 2005.
[21] H.-R. Zhang, Y.-C. Liu, T. Meng, Q.-P. Qin, S.-F. Tang, Z.-F. Chen, B.-Q. Zou, Y.-N. Liu, H. Liang, Cytotoxicity, DNA binding and cell apoptosis induction of a zinc(ii) complex of HBrQ, MedChemComm, 6 (2015) 2224-2231.
[22] H.-Y. Rao, J. Tao, S.W. Ng, Polymeric di-aqua-8-hydroxy-quinolinyl-5-sulfonatozinc(II), Acta Crystallogr. E: Crystallogr. Commun., 59 (2003) m859-m860.
[23] J. Tan, X. Li, Y. Zhan, J. Xiong, X. Lv, C. Pan, Y. Huo, Organic solvents-soluble zinc(II) and cadmium(II) complexes based on 2-aryl substituted-8-hydroxyquinoline: Synthesis, crystal structures, photoluminescence, thermal and theoretical studies, Polyhedron, 155 (2018) 398-406.

[24] I. Correia, J.C. Pessoa, M.T. Duarte, R.T. Henriques, M.F.M. Piedade, L.F. Veiros, T. Jakusch, T. Kiss, A. Dornyei, M.M.C.A. Castro, C.F.G.C. Geraldes, F. Avecilla, N,N '-ethylenebis(pyridoxylideneiminato) and N,N-ethylenebis(pyridoxylaminato): Synthesis, characterization, potentiometric, spectroscopic, and DFT studies of their vanadium(IV) and vanadium(V) complexes, Chem. Eur. J., 10 (2004) 2301-2317.
[25] P. Nunes, I. Correia, F. Marques, A.P. Matos, M.M.C. dos Santos, C.G. Azevedo, J.-L. Capelo, H.M. Santos, S. Gama, T. Pinheiro, I. Cavaco, J.C. Pessoa, Copper Complexes with 1,10-Phenanthroline Derivatives: Underlying Factors Affecting Their Cytotoxicity, Inorg. Chem., 59 (2020) 9116-9134.
[26] J. Costa Pessoa, I. Correia, Misinterpretations in Evaluating Interactions of Vanadium Complexes with Proteins and Other Biological Targets, Inorganics, 9 (2021) 17.
[27] A. Levina, D.C. Crans, P.A. Lay, Speciation of metal drugs, supplements and toxins in media and bodily fluids controls in vitro activities, Coord. Chem. Rev., 352 (2017) 473-498.
[28] A. Bujacz, K. Zielinski, B. Sekula, Structural studies of bovine, equine, and leporine serum albumin complexes with naproxen, Proteins, 82 (2014) 2199-2208.
[29] G.M. Sheldrick, SHELXT - Integrated space-group and crystal-structure determination, Acta Crystallogr. A: - Found. Adv., 71 (2015) 3-8.
[30] G.M. Sheldrick, Crystal structure refinement with SHELXL, Acta Crystallogr. Sect. C: Struct. Chem., 71 (2015) 3-8.
[31] L.J. Farrugia, *WinGX* suite for small-molecule single-crystal crystallography, J. Appl. Cryst. 32 (1999) 837-838.
[32] C.F. Macrae, I.J. Bruno, J.A. Chisholm, P.R. Edgington, P. McCabe, E. Pidcock, L. Rodriguez-Monge, R. Taylor, J. van de Streek, P.A. Wood, Mercury CSD 2.0 - new features for the visualization and investigation of crystal structures, J. Appl. Cryst., 41 (2008) 466-470.
[33] A.L. Spek, Single-crystal structure validation with the program PLATON, J. Appl. Cryst., 36 (2003) 7-13.
[34] APEX3, in: A. Bruker-AXS, in, Bruker AXS, Madison, Wisconsin (Ed.), USA, 2014.
[35] Bruker AXS: SAINT+, release 6.22. Bruker Analytical Systems: Madison,WI 2014.
[36] G.M. Sheldrick, A short history of SHELX, Acta Crystallogr. A, 64 (2008) 112-122.
[37] M.J. Frisch, G.W. Trucks, H.B. Schlegel, G.E. Scuseria, M.A. Robb, J.R. Cheeseman, G. Scalmani, V. Barone, G.A. Petersson, H. Nakatsuji, X. Li, M. Caricato, A.V. Marenich, J. Bloino, B.G. Janesko, R. Gomperts, B. Mennucci, H.P. Hratchian, J.V. Ortiz, A.F. Izmaylov, J.L. Sonnenberg, Williams, F. Ding, F. Lipparini, F. Egidi, J. Goings, B. Peng, A. Petrone, T. Henderson, D. Ranasinghe, V.G. Zakrzewski, J. Gao, N. Rega, G. Zheng, W. Liang, M. Hada, M. Ehara, K. Toyota, R. Fukuda, J. Hasegawa, M. Ishida, T. Nakajima, Y. Honda, O. Kitao, H. Nakai, T. Vreven, K. Throssell, J.A. Montgomery Jr, J.E. Peralta, F. Ogliaro, M.J. Bearpark, J.J. Heyd, E.N. Brothers, K.N. Kudin, V.N. Staroverov, T.A. Keith, R. Kobayashi, J. Normand, K. Raghavachari, A.P. Rendell, J.C. Burant, S.S. Iyengar, J. Tomasi, M. Cossi, J.M. Millam, M. Klene, C. Adamo, R. Cammi, J.W. Ochterski, R.L. Martin, K. Morokuma, O. Farkas, J.B. Foresman, D.J. Fox, Gaussian 16 Rev. B.01, in, Wallingford, CT, 2016.
[38] J.D. Chai, M. Head-Gordon, Long-range corrected hybrid density functionals with damped atom-atom dispersion corrections, Phys. Chem. Chem. Phys., 10 (2008) 6615-6620.
[39] D. Jacquemin, E.A. Perpète, I. Ciofini, C. Adamo, Assessment of the ωB97 family for excited-state calculations, Theor. Chem. Acc., 128 (2011) 127-136.
[40] J. Sabolovic, M. Ramek, M. Markovic, Calculating the geometry and Raman spectrum of physiological bis(L-histidinato)copper(II): an assessment of DFT functionals for aqueous and isolated systems, J. Mol. Model., 23 (2017).

[41] K.B. Wiberg, Basis set effects on calculated geometries: 6-311++G** vs. aug-cc-pVDZ, J. Comput. Chem., 25 (2004) 1342-1346.
[42] M. Gray, J.M. Herbert, Comprehensive Basis-Set Testing of Extended Symmetry-Adapted Perturbation Theory and Assessment of Mixed-Basis Combinations to Reduce Cost, J. Chem. Theory Comput., 18 (2022) 2308-2330.
[43] J. Tomasi, B. Mennucci, R. Cammi, Quantum mechanical continuum solvation models, Chem. Rev., 105 (2005) 2999-3093.
[44] O. Trott, A.J. Olson, Software News and Update AutoDock Vina: Improving the Speed and Accuracy of Docking with a New Scoring Function, Efficient Optimization, and Multithreading, J. Comput. Chem., 31 (2010) 455-461.
[45] J. Eberhardt, D. Santos-Martins, A.F. Tillack, S. Forli, AutoDock Vina 1.2.0: New Docking Methods, Expanded Force Field, and Python Bindings, J Chem Inf Model, 61 (2021) 3891-3898.
[46] E.F. Pettersen, T.D. Goddard, C.C. Huang, G.S. Couch, D.M. Greenblatt, E.C. Meng, T.E. Ferrin, UCSF chimera - A visualization system for exploratory research and analysis, J. Comput. Chem., 25 (2004) 1605-1612.
[47] M.F. Sanner, Python: A programming language for software integration and development, J. Mol. Graph. Model., 17 (1999) 57-61.
[48] V. Ferretti, C.P. Matos, C. Canelas, J.C. Pessoa, A.I. Tomaz, R. Starosta, I. Correia, I.E. León, New ternary Fe(III)-8-hydroxyquinoline-reduced Schiff base complexes as selective anticancer drug candidates, J. Inorg. Biochem., 236 (2022) 111961.
[49] B. Sergi, I. Bulut, Y. Xia, Z.A.E. Waller, Y. Yildizhan, C. Acilan, R.M. Lord, Understanding the Potential Modes of Action of Bis(β-diketonato) Oxovanadium(IV) Complexes, Chemmedchem, 16 (2021) 2402-2410.